

The Pennsylvania State University

The Graduate School

Eberly College of Science

**DYE-SENSITIZED SOLAR CELL FABRICATION AND
LIGHT TRAPPING MODIFICATIONS**

A Thesis in

Chemistry

by

Stuart Aaron Friesen

© 2013 Stuart Friesen

Submitted in Partial Fulfillment
of the Requirements
for the Degree of

Master of Science

August 2013

The thesis of Stuart Friesen was reviewed and approved* by the following:

Thomas E. Mallouk
Evan Pugh Professor of Materials Chemistry and Physics
Thesis Adviser

Karl T. Mueller
Professor of Chemistry

Raymond E. Schaak
Professor of Chemistry

Barbara Garrison
Shapiro Professor of Chemistry
Head of the Department of Chemistry

*Signatures are on file in the Graduate School

ABSTRACT

The objective of this study was to design and build sensitized, porous semiconductor films composed of two optically different but mechanically fused planar layers, ordered 200 to 600nm and disordered 25nm semi-crystalline TiO₂, in order to identify specific light wave scatterings, interferences and resonances within (i.e. Wood's anomalies, cavity resonators, slow photon propagation, Anderson localizations, etc). Since robust, reliable construction methods for bilayer dye-sensitized solar cells (bi-DSSCs) fosters consistency in performance from cell to cell and a higher signal-to-noise ratio during photovoltaic action, which in turn aids in examining the single variable of interest, robust and experiment-tailored fabrication methods for producing bilayer dye-sensitized solar cell evolved into the main focus of this study.

Three different bi-DSSC fabrication categories were pursued: 1) decal transfer of one layer onto the other; 2) build inverse opal (IO) directly on top of a mesoporous nanocrystalline TiO₂ (meso ncTiO₂) film; and, 3) build the meso ncTiO₂ layer directly on top of an IO layer. Experimental observations of morphology, spectral responses and light-to-energy responses were made on all attempts to construct bi-DSSCs but none of the attempted methods proved successful for joining these two layers. An ncTiO₂ particle infiltration into colloidal crystal template infiltration method is believed to be the most consistent and flexible IO layer fabrication method for bi-DSSCs. Isolation of the majority of pores within a meso nc-TiO₂ film by way of atomic layer deposition (ALD) of Al₂O₃ onto the meso nc-TiO₂ film's outer surface followed by ion mill leveling is believed to be an effective method for bi-DSSC fabrication systems 1 and 2, above. It appears most useful for direct deposition of a colloidal crystal and subsequent infiltration with nc-TiO₂ particles and/or a decal technique involving a milled IO layer attached to the Al₂O₃ protected meso nc-TiO₂ using a newly developed TiO₂ sol-gel that can form a meso film within submicron confined spaces and thus "glue" the two separately prepared films together.

Due to a noticeable lack of easily accessible, easy-to-follow and complete guides to understanding and fabricating moderately efficient, ~6.5%, DSSCs, one was developed. It provides a quicker initiation into laboratory-grade DSSC building and testing without cumbersome steps such as dye purification, light scattering layer addition or ncTiO_2 sol pretreatment of FTO or post treatment of the photoanode. Since DSSCs are relatively easy to fabricate, morphologies are easily altered and involve much less lab equipment than do other solar cells, providing this guide will be very useful for solar cell research in general at the undergraduate level as it facilitates less of an investment of time to get started.

TABLE OF CONTENTS

LIST OF FIGURES	v
LIST OF TABLES	viii
Chapter 1. Background and Introduction	1
1.1. Current Outlook on Photovoltaics' Role in the Energy Market	1
1.2. Enhancing the Dye-Sensitized Solar Cell's Performance	6
1.3. General Experimental Goals and Strategies	9
Chapter 2. Robust Laboratory Methods for Dye-Sensitized Solar Cell Fabrication and Performance Testing	12
2.1 Overview of Dye-Sensitized Solar Cell Laboratory Investigation	12
2.2 Overview of a Standard DSSC Functional Design	16
2.3. Guide to Understanding Photovoltaic Mechanisms	19
2.4. Guide to Characterizing the Photovoltaic Performance	29
2.5. Guide to Building Robust Laboratory DSSCs	35
2.6. Detailed Descriptions of DSSC Components	48
Chapter 3. Coupling an Inverse Opal to a Mesoporous Semiconductor Layer	58
3.1. Overview of Photonic Crystal Coupled DSSCs	58
3.2. How a Photonic Crystal Guides Light Waves	61
3.3. Strategies for Building bi-DSSCs	63
3.4. Choice of bi-DSSC Materials	65
3.5. Experimental bi-DSSC Attempts	65
3.6. Conclusions and Future Work	80
Appendix	82
References	84

LIST OF FIGURES

Figure 1-1: Contribution and value of electricity sources to the market.....	3
Figure 1-2: Formation of meso layer in viscous polymer versus 3D-PC layer	11
Figure 2-1: Unique DSSC organic-inorganic semiconductor PV material	15
Figure 2-2: View of a DSSC with labeled components.....	17
Figure 2-3: View of light scattering layer on top of meso nc-n-Sc film.....	17
Figure 2-4: DSSC Photoelectrochemistry.	20
Figure 2-5: Electronic Potential Energy Levels of a std-DSSC.....	21
Figure 2-6: Bohr-like Atom Absorbing a Photon's Energy.....	24
Figure 2-7a: Discrete oscillatory frequencies of 2-D standing waves.....	25
Figure 2-7b: Depiction of a simple 3-D standing wave.....	25
Figure 2-8: Rates of interfacial electron transfer.....	26
Figure 2-9: Maximum power point of solar cell under illumination.....	31
Figure 2-10: Power Curve for DSSC under one sun AM 1.5 conditions.....	32
Figure 2-11: Incident photon-to-current conversion efficiency curve.....	33
Figure 2-12: DSSC without light scattering layer on the right and bi-DSSC on the left.....	34
Figure 2-13: Normalized <i>IPCE</i> spectra at 535nm	35
Figure 2-14: Hydrolysis and peptization steps in same round bottom.....	38
Figure 2-15: <i>IPCE</i> spectra of an N719 dyed std-DSSC with ARKTOP.....	49
Figure 2-16: SEM image of the top of a FTO film deposited on glass.....	50
Figure 2-17: Transmittance spectra of FTO with and without a TiO ₂ barrier layer	51
Figure 2-18: FESEM image of blocking layer.....	52
Figure 2-19: SEM cross-sectional image of mesoporous nc-n-TiO ₂ film	53
Figure 2-20: TEM image of TiO ₂ nanocrystalline particles.....	54

Figure 2-21: High Performance DSSC Sensitizers; YD2- <i>o</i> -C8, N719 and Black-Dye.....	55
Figure 2-22: Sensitizers' Absorption Spectra; N719, Black-Dye and YD2- <i>o</i> -C8.....	56
Figure 3-1: 3D photonic crystal coupled DSSC.....	58
Figure 3-2: Illustrations of 3D-PC DSSC and bi-DSSC.....	59
Figure 3-3: Resonant wave guiding in a cavity causes light localization.....	60
Figure 3-4: Inverse opal <i>fcc</i> crystal.....	61
Figure 3-5: Depiction of 3D-PC diffraction cone formation and intersection.....	62
Figure 3-6: Standing waves at blue and red edges of the forbidden gap at the 1 st Bragg plane...63	
Figure 3-7: Absorption curve for 300 and 400nm Inverse Opals.....	64
Figure 3-8: (a) Overlayer on top of TiO ₂ inverse opal (1,1,1) surface	67
Figure 3-9: Unit cell for <i>fcc</i> crystal. Inverse opal <i>fcc</i> unit cell.....	69
Figure 3-10: TiO ₂ Sol-gel infiltrated colloidal crystal after RIE treatment.....	71
Figure 3-11: (a) IO top before RIE. (b) 45 sec RIE.....	72
Figure 3-12: (a) IO top before RIE. (b) 45 sec RIE.....	72
Figure 3-13: Ion milled.....	73
Figure 3-14: 45sec RIE sol-gel infiltrated PS colloidal crystal	74
Figure 3-15: 320nm void diameter inverse opal on PVA; RIE 30 sec. Before decal transfer ...	75
Figure 3-16: 320nm void diameter bi-DSSC	76
Figure 3-17: a) IO layer decal film sintered to meso nc-TiO ₂ layer. (b) FIB trenching.....	76
Figure 3-18: Spin coat nc-Al ₂ O ₃ /nc-TiO ₂ 1:1 mix.....	77
Figure 3-19: Sandwiched PC template infiltrated with 6-10nm nc-TiO ₂ particles.....	77
Figure 3-20: PC template infiltrated with 6-10nm nc-TiO ₂ particle colloidal solution.....	78
Figure 3-21: Screen print nc-Al ₂ O ₃ /nc-TiO ₂ 1:1 mix w/ binder.....	79
Figure 3-22: Meso-ncTiO ₂ layer coated with Al ₂ O ₃ by ALD	79
Figure A-1: Advances in solar cell types: Efficiency versus year chart, from Ref 11.....	82

Figure A-2: Absorption Spectrum of N719 Dye.....83

LIST OF TABLES

Table 1-1: Projected levelized cost generated electricity of resource- (\$/MWh) in 2018.....	2
Table 2-1: Main Function(s) of Each Functional DSSC Component.....	18
Table 2-2: Table 2-2. Materials list for 5mL of I^-/I_3^- electrolyte.....	46

Chapter 1. Background and Introduction

1.1. Current Outlook on Photovoltaics' Role in the Energy Market

As our population and per capita desire for energy continue to grow globally, our energy generation capacity will necessarily evolve. Selecting sources of energy that best serve our future, however, presents a complex puzzle. At the foreground of energy development are economic and technological constraints. But increasingly prevalent are the various ramifications of developing and utilizing particular energy resources. Most impactful are the environmental effects associated with energy generation. For example, increases in greenhouse gas emissions (GHGEs) have been found to impact our global ecosystem to the point of impending disasters.¹ Consequential are international relations with fossil fuel producers; peaceful ties between producer and consumer countries have grown sensitive and susceptible to discord.² Fortunately conventional energy production system alternatives, such as photovoltaic (PV), biomass, geothermal and wind, are being developed. Because it is an attractive and potentially good candidate for penetrating the forthcoming electricity market, PV's role and viability in it will be examined in the following.

Between 2008 and 2011 the capacity of solar generated electricity rose 380% worldwide. In sharp contrast to its impressive growth spurt, however, is the minor portion of globally consumed electricity supplied by PVs during 2011: just 0.28% worldwide (61.6 of 21,964 TWh)³; and a mere 0.04% of the U.S. electricity mix. This disparity raises several critical questions concerning PV's evolution and penetration into the upcoming market. Will PV capacity continue to be cultivated, and at what pace? Or, will its development be stunted by high supply cost

(\$/kWh) and intermittency? And, what sort of changes would need to and could materialize in order to consummate a more substantial integration of PVs into the electricity supply mix?

Their relatively low capacity factor⁴ and traditionally high cost have certainly prevented conventional PV farms from supplying consumers with the most reliable, lowest-cost electricity. As shown in Table 1 several established technologies, such as coal, natural gas (collectively referred to as fossil fuels) and hydraulic have generated and delivered electricity at considerably lower levelized costs⁵ and higher capacity factors. Figure 1(b) combines Table 1 with Figure 1(a) to convey a correlation between the apparent value of each key resource-to-electricity industry and each industry's percentage of the electricity market. Figure 1(b) reflects common sense business practice: the more dependable and economically processable the resource, the more extensively it is utilized and thus valued in marketplace. Furthermore Figure 1(b) reveals a conspicuously low value as well as a high potential growth barrier for PVs.

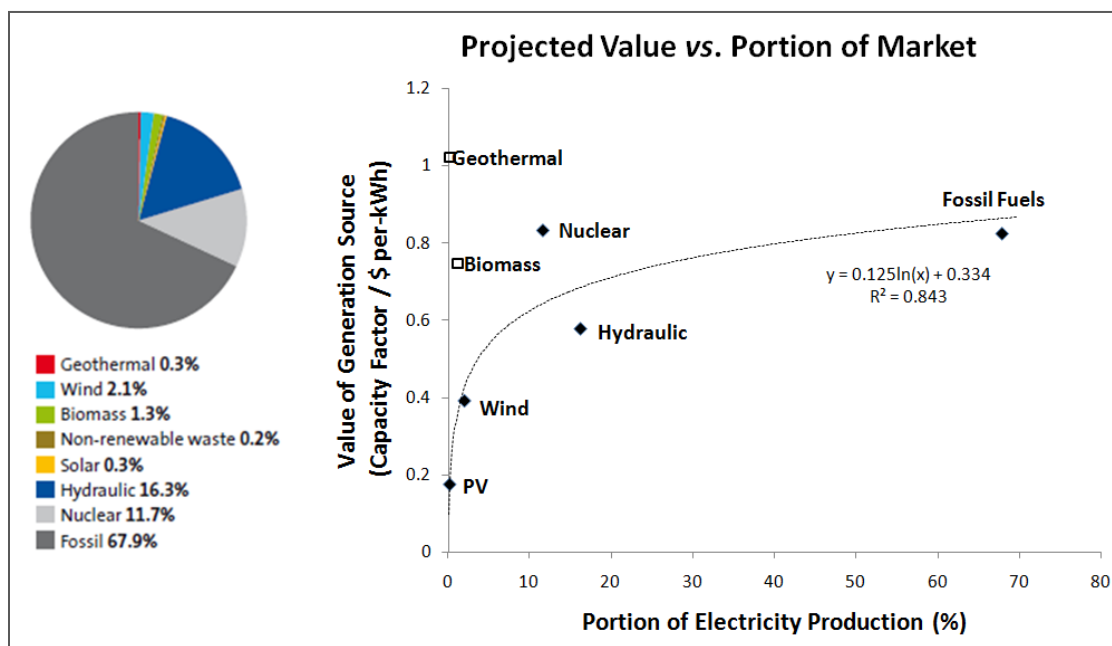
Table 1-1: Projected levelized cost generated electricity of resource- (\$/MWh) in 2018.

Electricity Generation	Cost (\$ per-MWh)	% Less than PV	Capacity Factor (%)
Photovoltaic	144	0	25
Clean Coal w/CO ₂ Sequestration	136	6	85
Clean Coal	123	15	85
Conventional Coal	100	31	85
Biomass	111	23	83
Hydraulic	90	38	52
Wind	87	40	34
Geothermal	90	38	92
Natural Gas w/ CO ₂ Sequestration	93	35	87
Conventional Natural Gas	67	53	87

Note: The cost of each electric source is compared to PV: % less than PV = [(cost of PV – cost of other source) ÷ cost of PV] x 100%. Capacity Factor= [(full capacity (MW) x full time generation (hr)) ÷ (averaged capacity (MW) x actual generation time (hr))] × 100%.

Expectedly this trend is very persuasive and thereby compels one to conclude that expanding PV capacity appears relatively imprudent and prohibitive while, on the other hand, nuclear, geothermal and biomass, wise. Future investments in PV, or any other resource-to-

electricity manufacture, however, cannot be properly analyzed and evaluated from a single snapshot of its extant performance in a dynamic market as it narrowly excludes context and viability. The fact remains that the futures of PV and other power harnessing systems evolve from a complex, multivariate sequence or convergence of social, political, economic, environmental and technological developments which can impact all or some of the resource-to-electricity processing steps (system development and construction, resource collection and conversion and power delivery).



1(a) Portions of electrical production sources worldwide in 2011. Note: fossil fuel is mainly comprised of coal and natural gas. 1(b) Apparent value of electricity generation source (the quotient of capacity factor and projected 2018 supply cost (\$/kWh)) versus portion of 2011 production worldwide.

Figure 1-1: Contribution and value of electricity sources to the market.

For example, to date data show that nuclear strays from the above value vs. utilization trend; utilization of nuclear is disproportionately low compared to its well established high value. The underlying circumstances behind its displaced capacity have historically been social apprehension towards the persisting fatal consequences of meltdowns and improper waste management. This combined with the large, government-backed investments needed for its

development have created a substantial socio-political barrier retarding nuclear from reaching its calculable potential. Unfortunately the release of deadly radioactive material from the Fukushima Daiichi and Chernobyl plants in 2011 and 1986, respectively, and the recent leaking and looting of nuclear waste from sustained storage facilities are likely to pervade society's conscience with a foreboding outlook on nuclear power augmentation for some time to come.

Just as socio-political perceptions can proscribe nuclear expansion, exploration technology can impede geothermal development. Similarly veiled in Figure 1(b) is the fact that geothermal-to-electricity plants proficient at supplying presently low cost and reliable energy are limited to locations near tectonic plate boundaries where reservoirs of core-to-crust heat conduction media clearly manifest on the earth's surface. Detecting viable, undiscovered geothermal pockets has proven technologically very challenging and as a consequence financially risky. However, if recent research findings are valid, new cost-effective methods for detection using remote sensing may be just around the corner.⁶ Should this be the case, the extant performance data would correctly herald investments towards developing this resource. Nonetheless, the viability of geothermal growth will be based on how effectively this new technology can be implemented and not on the encouraging portrait granted by a performance data.

Likewise, the most cost-effectively manufactured resource, conventional natural gas (Table 1), has several hidden caveats. Conventional and economically extractable reserves are dwindling, and at a particularly fast pace in the U.S. Natural gas extraction in the U.S. has not declined, however, because caches of gas trapped in shale deposits have thus far been cost-effectively withdrawn using hydraulic fracturing and horizontal drilling technology; in 2011 36% of the $7.9 \times 10^{11} \text{ m}^3$ of natural gas consumed in the U.S. came from shale caches⁷. Nonetheless the known aggregate of reservoirs in the U.S. have a finite supply (estimated at $\sim 62 \times 10^{12} \text{ m}^3$; the

current consumption rate is $\sim 70 \times 10^{10} \text{ m}^3/\text{yr}$). Ultimately limited supply will impact the capacity of natural gas-to-electricity generation.

Furthermore, emerging economic and environmental issues surrounding shale gas extraction and subsequent gas-to-electric production will impact shale gas processing costs in the near future. Due to recent over-speculation of shale gas, the price of natural gas in the U.S. is expected to rise by as much as 67%. Additionally 4 to 8% of the extracted shale gas is released to the atmosphere where its main constituent, methane, poses a high potential threat to the greenhouse gas (GHG) effect.

On the other hand, economic, socio-political and technological factors are currently working in favor of augmenting PV capacity and lowering its cost (hence raising its market value). In 2012 taxes and incentives for the development of renewable energy supply systems were offered by twenty-three countries around the world.⁸ In the U.S. 30% federal tax credits on newly installed and operating residential PV systems before 2017 are available; additional state and local incentives further lower the cost of solar systems.⁹ These incentives in concert with the recently lowered purchase prices (below \$1/W) for $\geq 15\%$ efficient single crystal silicon (c-Si) and polycrystalline silicon (p-Si) PV modules have resulted in a recent spike in solar system installations across the U.S. Efforts towards reducing GHG emissions responsible for catastrophic changes in global climate have been gaining more and more support by the general public. For example, the World Bank president, Jim Yong Kim, released a report in 2012 stating that the World Bank recognizes the impending severe climate changes caused by increases in GHG emissions and the disastrous effects they will impose on worldwide economic prosperity. Finally, technological advances have been continually increasing light-to-power conversion efficiencies of many solar cell types as well as decreasing manufacturing costs.

Silicon p-n junction PVs (Si-PVs) are the current, predominant light-to-energy conversion apparatus. Their efficiency is high in terms of Whrs / m^2 as is their energy value in

terms of \$ / W. However, opportunities for other solar cells to advance in the emerging market are opening because of recent drops in economy of scale for single crystal Si PV, which is due to persistent declines in the demand for computer circuitry parts. The most efficient single junction PV, GaAs, could certainly stand to gain more penetration into the solar market. Research into Si-PV alternatives such as thin film PVs has increased as have their performance efficiencies. The most promising thin film PVs for commercial development are: Heterojunction with intrinsic thin layer (HIT), Cu[In,Ga]Se₂ (CIGS), CdTe, organic bulk-heterojunction and dye-sensitized solar cell (DSSC) PVs; see Figure A-1 for a PV efficiency versus research time profile.

Organic bulk-heterojunction and DSSCs can be produced by low cost and highly scalable manufacture methods. However, these cells are only moderately efficient and thus do not yet rank high in terms of market energy supply values. DSSCs have in particular been subject to a lot of research because of the many opportunities that this type of multi-component cell offers for power generation performance enhancement. DSSCs also tend to perform at high open-circuit voltages (V_{oc}).

Relatively high tax-payer incentives for PV power production, increasing performance efficiencies of alternatives to Si-PV, and the availability of advanced electrical grid controllers (i.e. SMARTGRID) have significantly contributed to the current public's wider acceptance of solar power generator systems. DSSC production is very economically scalable and is likely to increase in the near future.

1.2. Enhancing the Dye-Sensitized Solar Cell's Performance

A standard dye-sensitized solar cell (std-DSSC) has a moderate light-to-power conversion efficiency (η) compared to the market dominant c-Si and p-Si single p-n junction PVs. Under one sun (1mW/mm²) and AM 1.5 conditions, average Si-PV modules perform at $\eta \geq 15\%$

while prototypical std-DSSC modules produce electricity at $\eta = 7\%$.¹⁰ Despite this shortcoming,¹¹ extensive research dedicated to understanding and developing the std-DSSC, and modified versions of it, has been pursued for more than two decades. Inquiries have so far significantly contributed to enhancing std-DSSC efficiencies as well as advancing solar cell, molecular, electrochemical and materials science knowledge.¹² Continuing investigations, despite DSSC's present lack of efficiency status, will likely benefit solar technology and science in general even further.

The DSSC's unique light-to-energy conversion processes, materials and efficiency parameters make this cell a rich source of study. Like the chloroplast, a DSSC is a finely balanced and integrated compilation of various components; changing a single component can upset or enhance DSSC performance depending on compatibility and optimization factors; Figure 2-2. Like a chloroplast's granum with its exceptionally high surface area-to-volume ratio, the mesoporous photoanode, a sponge-like structure of sintered polycrystalline semiconductor nanoparticles, is one of the DSSC's principal constituent. It provides an ideal scaffold for inflowing light to be maximally absorbed within a thin film's shallow depth and without requiring expensive and highly purified semiconductor material. Furthermore, methods for processing these photoanodes are facile, economical and flexible, and thus supply extensive opportunities to fabricate novel composite structures.

One such alternative photoanode, the photonic crystal coupled or bilayer DSSC (bi-DSSC) is designed to increase the sensitizer's absorbance of the solar spectrum by way of amplifying and localizing its electric fields within the cell. The bi-DSSC consists of a mesoporous semiconductor layer welded to a 3-D photonic crystal (3D-PC) layer; Figure 3-1. Electromagnetic waves, whose lengths are on the order of the spacing between scattering centers of the 3D-PC, interact with the periodically arranged dielectrics. Because of diffraction, bands of light are forbidden to propagate through the 3D-PC; these are called photonic band gaps. Due to

the thickness of the 3D-PC slab in a typical bi-DSSC, as well as lack of contrast between the operating dielectrics, however, the photonic band gap is not complete across all the angles of incidence. This type of forbidden gap is therefore called a pseudo photonic band gap or stop band; Figure 3-6.

The thickness of the 3D-PC can also be detected using reflection spectroscopy. If 3D-PC film is thin, the period, T , of the Fourier transform, F , cannot approach infinity (which would represent infinite scattering events within the 3D-PC). Consequently the frequency range, $\Delta\xi$, of light waves entering the 3D-PC from a given angle and experiencing multiple scattering events, according to Equation [1], will increase as T decreases. Therefore a reflection spectrum of a thin 3D-PC would display a wide stop band (Figure 3-7) conversely a narrow stop band would be seen as T approaches ∞ . In the below equation t is time and n is series.

$$f(t) = \frac{1}{T} \sum_{n=-\infty}^{\infty} F(n/T) e^{2\pi i \left(\frac{n}{T}\right) t} = \sum_{n=-\infty}^{\infty} F(\xi_n) e^{2\pi i \xi_n t} \Delta\xi \quad [1]$$

When light whose energy lies within the stop band tries to propagate through the 3D-PC, the light is scattered incoherently out in many angles and/or coherently back out from where it came. Some of this back-reflected light is thought to be captured in effective resonant cavities created within the mesoporous film²⁶. Under this condition optical energy would be temporally and spatially confined. Understanding the conditions in which this type of resonance effect occurs in a bi-DSSC, therefore, would lead to more effective light trapping; especially since confined propagation occurs or near the meso nc-n-SC layer, which is most densely populated with sensitizer molecules.

Additionally photons that have energies near one of the edges of a stop band will, because of the dispersion relation, resemble a standing wave as its group velocity is close to zero, $v_G = \frac{d\omega}{dk} \cong 0$; Figure 3-6. Inside the 3D-PC the confinement of these slow photons resembles an oscillating string between two fixed points when a standing wave is formed. Those

electromagnetic waves whose energies lie near the blue edge of the stop band constructively interfere in their forward and reverse propagating paths. These waves oscillate with nodes at the high refractive index material, i.e. semiconductor. Conversely waves oscillating in the 3D-PC with frequencies near the red edge of the stop band have nodes at the low refractive index material, i.e. redox couple medium. Thus electric field enhancement occurs at both edges of the stop band but in opposing media.

In other words, as a result of light's interactions with the bi-DSSC's photoanode, the paths of select incoming photons are detoured. And by altering the paths of incoming photons with a 3D-PC, the photons are either retained, dampened or amplified, to varying degrees, within the cell. Thus, by increasing the amount of confined and resonant modes for light waves absorbable by the sensitizer (but by less than 60% of unity), the number of photogenerated electrons per unit time, or photocurrent, producible by the bi-DSSC would increase.

1.3. General Experimental Goals and Strategies

The motivation for these studies was to develop a robust method for fabricating bi-DSSCs in pursuit of investigating the correlations between relevant physical characteristics of a bi-layer composite film and light wave localizations and resonances within the subsequent bi-DSSC. The majority of resonances and localizations in bi-DSSCs are initiated by multiple Mie scattering events at and within the 3D-PC. Subsequent light wave interferences and localizations develop within both layers of the composite photoanode. The photoanode characteristics most relevant to inquiries about observable relationships between structure and specific light-matter interactions are: the stop bands of the 3D-PC and bi-layer composite films; the morphology of the meso nc-n-SC/3D-PC interface; the macro and micro morphologies, mean free path length of light, l_{mfp} , distances between scattering centers, d , and volume fraction, f , of the 3D-PC

backbone; the morphology of the meso nc-n-SC film; and, thicknesses and specific surface areas of each film type. Once composite photoanode films can be reliably fabricated and altered, according to the needs of a specific investigation, the door opens for exploring the light-matter interactions that most benefit the light-to- power performance efficiency of a bi-DSSC.

To the best of my knowledge, only one purported bi-DSSC fabrication method involving atomic layer deposition (ALD) deposition of TiO_2 into the opal template's interstices is robust.¹³ However it is not very flexible and thus may not be amenable to the types of inquiries that elucidate an understanding of light-matter interactions occurring within bi-DSSCs. Nonetheless, a suitable method for processing robust bi-DSSCs proved unattainable based on our many attempts, deeper insight into the specific challenges that need to be overcome in order to successfully construct reproducible bi-DSSCs according to specific experimental needs was vastly illuminated. The elusiveness encountered while attempting to consistently and completely fuse these two layers into a single, composite bi-layer film was primarily a result of the disparate processes typically used to form each film type; Figure 1-2. The mesoporous film is cast from a thick suspension of nanocrystalline n-type semiconductor (nc-n-SC) particles suspended in a polymer matrix (called the nc-n-SC paste). Contrastingly the 3D-PC is constructed from two separate wet chemical processes: 1) depositing a sacrificial opal template by evaporative colloidal assembly of nanospheres, Figure 1-2b; 2) and, infiltrating the resultant fcc colloidal crystal with either a metal oxide sol-gel or a dilute colloidal solution of small nc-n-SC particles. Additionally the two layers have incompatible coefficients for expansion and contraction; for example when forming an inverse opal, a sol-gel infiltrated colloidal crystal shrinks anisotropically calcined (~ 10 to 15% laterally and 20 to 25%).

Three main routes towards building a fused bi-DSSC were pursued: 1) joining two films fabricated separately and previously; 2) depositing the 3D-PC onto the mesoporous layer; or 3) depositing the nc-n-SC paste onto the 3D-PC layer. The first option was problematic due to: the

unevenness of the surfaces to be mated; the large differential in thermal contractions and expansions of the two films during the calcination/sintering treatment; and, formation of a meso-nc-n-SC film within the confines of two planar surfaces. The second approach was also very challenging since the metal oxide sol-gel permeates the interstices of both layers when attempting to solely infill the fcc colloidal crystal. And the third presented the problem of electronically connecting the transparent conductive oxide (TCO) layer to an external circuit conductor.

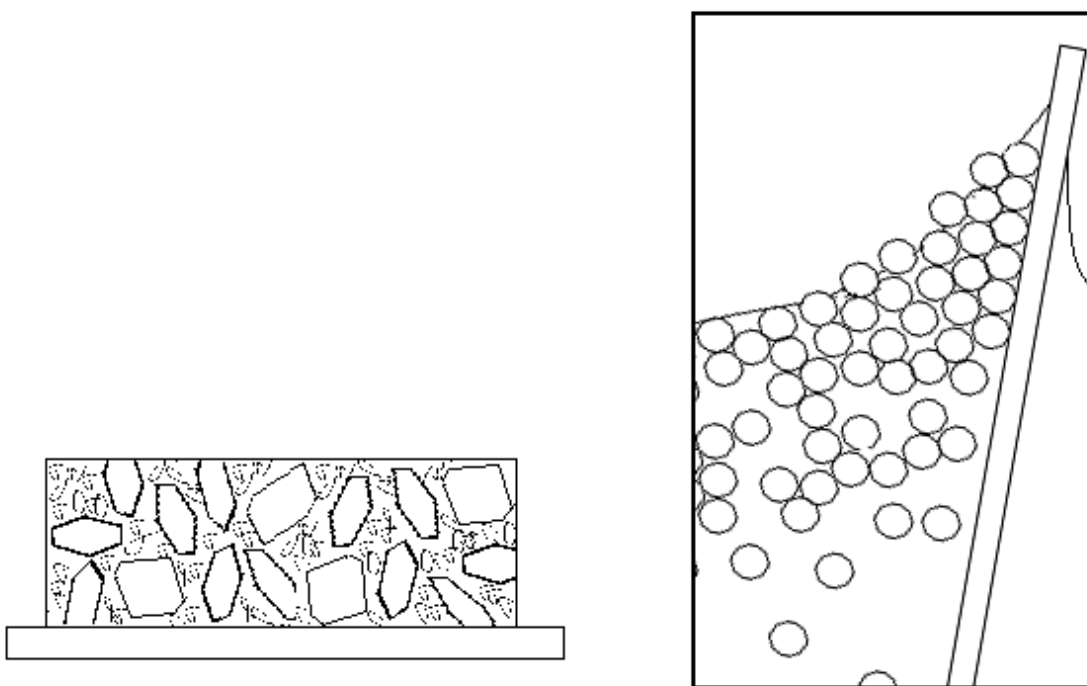


Figure 1-2: Formation of meso layer in viscous polymer versus 3D-PC layer in dilute colloidal solution.

Since the level of difficulty is inversely proportional to level of reproducibility with regard to a fabrication process, developing a reliable recipe for ensuring electronic connectivity between the two structurally and manufacturally dissimilar layers is, as explained, challenging. In practice, high reproducibility increases the physical constants present in all the bi-DSSC structures produced. In turn, variables to be studied, such as stop bands, are more isolatable, comparable and analyzable. Subsequently studies of bi-DSSCs have been thus far been limited in

scope. Reports typically contain data on the bi-DSSC's global and external quantum efficiencies, impedance and reflectance spectroscopy, and light enhancement factors. But no empirical study has yet been made on the unique types of light localization effects that can be specifically engineered by fusing these two layers.

While striving for a fabrication system of highly reproducible and flexible bi-DSSCs we found there lacked a publically available guide that comprehensibly explains the construction, design, and mechanistic principles of std-DSSCs, a foundational third generation solar cell. In the following chapter, DSSC fabrication and testing instructions coupled to a conceptual description of DSSC photon-to-electricity principles will be provided for those embarking on advanced DSSC investigations. In Chapter 3 the optical effects of 3D-PCs will be explained and the variety bi-DSSC assembly processes attempted will be presented and discussed in detail. And in the Summary section of Chapter 3 a proposed method for making bi-DSSCs will be described.

Chapter 2. Robust Laboratory Methods for Dye-Sensitized Solar Cell Fabrication and Performance Testing

2.1 Overview of Dye-Sensitized Solar Cell Laboratory Investigation

Fabricating and testing laboratory-grade DSSCs for their photovoltaic efficiencies is relatively easy and inexpensive, which makes them useful for investigating different aspects involved in its photovoltaic mechanism. Additionally, the diverse range of materials used for its components; the integral interactions between its components; and the flexibility with which components can be synthesized and assembled makes this third generation solar cell species ideal for an expansive variety of laboratory-type investigations. Advanced materials and physical

chemistry studies of solar cells, for example, would greatly benefit from including or even starring the DSSC in the lab.

This chapter provides an readily accessible collection of information useful for laboratory investigations of DSSCs: Section 2.2 is an overview of a std-DSSC and its components; Section 2.3 is a guide to understanding the mechanistic principles involved in a std-DSSC; Section 2.4 is a guide for fabricating a std-DSSC; Section 2.5 is a guide to std-DSSC performance testing equipment and procedures; and, Section 2.6 has detailed descriptions of each std-DSSC component.

2.1.1 Background of DSSC Investigations

The record global light-to-energy efficiency, η , for the highest performing laboratory std-DSSC is $\eta = 14.1\%$; Appendix 1A. While the equipment needed to produce this high grade cell is not trivial, it is not, however, necessary for developing and testing experimental ideas aimed at enhancing or modifying the std-DSSC performance. The seminal work of Mallouk et al. on bi-DSSCs stands as a good example. Without sophisticated DSSC fabrication equipment and techniques, this group explored the idea of enhancing the sensitizer's absorbance as a result of the photoanode's structure. By localizing and increasing the intensities of select ranges of light inside a three-dimensional photonic crystal (3D-PC) coupled to a DSSC's mesoporous semiconductor layer, Figure 3-1, the number of photons converted to electricity within the cell increased. The η of the DSSC and bi-DSSC constructed and analyzed by Mallouk et al. were multiples lower than the std-DSSC's η at that time. Nonetheless this group found that if its stop band is properly adjusted to the sensitizer's absorption spectrum, the 3D-PC effectively enhances the DSSC light harvesting efficiency, which in turn enhances the DSSC's overall performance. Additionally, since these published findings, many investigations have sought out various

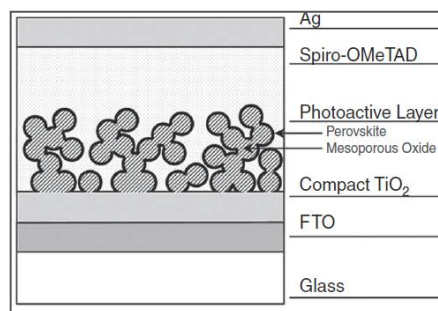
composite DSSC photoanode structures which have enhanced the public's understanding of solar cell performance using photonic crystal structures.^{14,15}

Improving one or more of the DSSC component(s) is certainly another logical route towards understanding and increasing cell performance. Nazeerudin et al. have done considerable work on developing sensitizers for the std-DSSC. Joined by a group specializing in DSSC redox pair material, the performance of a std-DSSC in the longer wavelength region of the solar spectrum was improved by using a porphyrin dye. Interestingly this dye is most effectively regenerated by a cobalt (II/III) tris(bipyridyl) redox pair. This publication punctuated the fact that each specific sensitizer, even variations of ruthenium dyes, must be matched to a particular redox couple or hole conductor in order to optimally function.

One outstanding feature of the porphyrin sensitized cell is its relatively high open circuit voltage, V_{oc} . The cobalt-based redox pair's high reduction potential (or low potential energy; Figure 2-13) enables the std-DSSC to reach a $V_{oc} = 935$ mV. Additionally the porphyrin molecule has a high absorption coefficient over a broad spectral range (Figure 2-22(b)) which, under favorable cell conditions, facilitates a high short-circuit current density, J_{sc} ; equation X. Resultantly this porphyrin-sensitized std-DSSC performs at $\eta = 12.3\%$.

The above studies demonstrate that there various possible strategies for fostering solar cell knowledge and progress. Viable strategies for increasing DSSC's performance can be: applying DSSC design principles to novel configurations such as Mallouk et al.; optimizing a compatible DSSC component as demonstrated by Nazeerudin et al.; or, by applying DSSC design principles to new materials and variant mechanistic principles. Snaith et al recently developed an organometal halide perovskite-sensitized solar cell which stands as an exceptional example to the latter tactic; Figure 2-1.¹⁶ Third generation solar cell criteria are well met by this novel PV cell; all materials are abundantly available while the active portion of the cell is very thin (approximately one micron). The mesoporous metal oxide photoanode supports a layer of very

cheap semiconductor material with a short optical absorption length (but also a very high absorbance coefficient). This very thin photoactive layer of perovskite semiconductor is thereby afforded a high absorption area-to-incident photon ratio by the almost transparent mesoporous scaffold. A one micron thick laboratory cell performs at $\eta = 10.9\%$.



Supersaturated organometal halide perovskite coats the metal oxide mesoporous layer. In this adaptation of the DSSC photoanode the metal oxide layer is not used to transport high potential electrons. Image was taken from Ref. 15.

Figure 2-1: DSSC's prominent high specific area metal oxide scaffold accommodates a unique organic-inorganic semiconductor PV material.

Regardless of which DSSC modification scheme is pursued, understanding the materials, fabrication process and, most importantly, the underlying design and mechanistic principles of a functional DSSC provide a springboard to transmutation. Step-by-step procedures involved in DSSC fabrication can be tailored to time and monetary constraints and, perhaps more importantly, specific research aims. On the other hand, achieving reliable photovoltaic performance tests and a sufficient understanding of DSSC design and mechanistic principles requires essential investments in equipment and time, respectively.

The rest of this chapter will serve as a bridge for those launching or extending DSSC experimentation. Section 2.2 supplies a broad description of the std-DSSC and its functional components. More detailed and informative descriptions of each functional part is provided in Sections 2.6.1 through 2.6.10; initially, this section can be initially skimmed in order to get a general sense of its contents since these sections will be referred to frequently throughout Chapter

2. Guides to DSSC operational mechanisms, fabrication methods for laboratory-grade DSSCs and DSSC photonic performance testing follow section 2.2, in that order. In Section 2.3 the operational design and mechanistic principles are discussed in simplified yet accurate terms; note that many of the references cited can provide more complete descriptions for deeper understandings. In Section 2.5 the fabrication section provides robust “recipes” for preparing and assembling DSSC components in order to make a functional cell that performs at a light-to-energy conversion efficiency of 6.5%. There are different ways or types of components that can be effectively used to make a DSSC. However, the descriptions of those used in our research are primarily provided in the following; some alternatives are mentioned in Section 2.6. Similarly, the performance testing section will include various options for testing equipment (i.e. a solar simulation system); how to test DSSCs; and, how to use the data acquired for revealing solid investigatory questions.

2.2 Overview of a Standard DSSC Functional Design

The functional parts of a standard DSSC (std-DSSC) fit into two broad categories: 1) light management; and, 2) charge management. As seen in Table 2-1, below, most of its contents serve both purposes. An orthogonal view of a std-DSSC is shown in Figure 2-2; for clear identification of its functional components the scatter layer is omitted. A scattering layer, which is half or less the thickness of the meso layer, is typically sintered onto the backside of the meso layer; Figure 2-3.

It is important to remember that the integrated nature of DSSC’s parts necessarily means that each one has an effect on and/or can be affected by the others. In order to best anticipate and design DSSCs in accordance with the interrelatedness of parts, it is very advantageous to have a

working understanding of each part and, more importantly, the photovoltaic mechanistic principles occurring within DSSCs; Section 2.3.

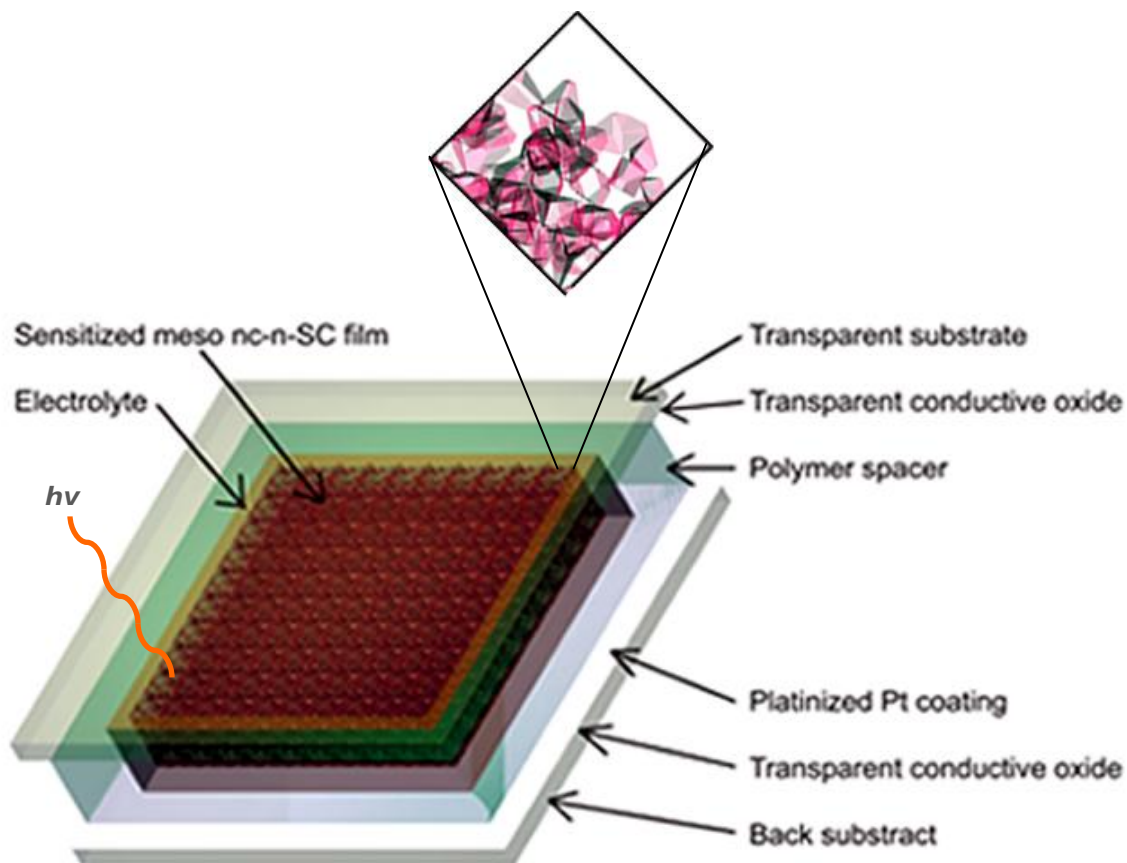


Figure 2-2: View of a DSSC with labeled components. Close-up view of sintered nc-n-SC particles.

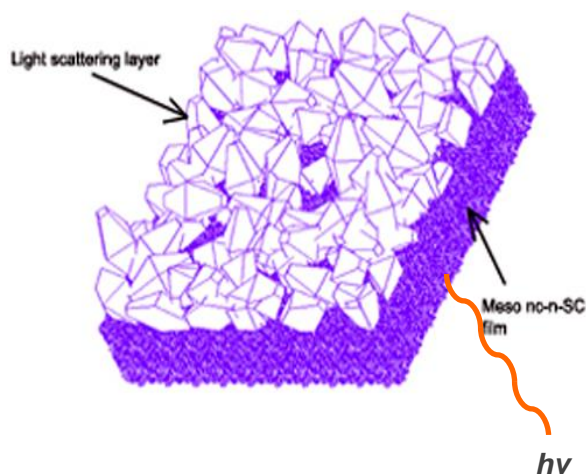


Figure 2-3: View of light scattering layer on top of meso nc-n-Sc film.

Table 2-1: Main Function(s) of Each Functional DSSC Component.

Component's Name	Manages		Main Function(s)
	Light	Charge	
Anti-Reflective Film	×		transitions light from air-to-substrate refractive indices
Transparent Substrate	×		light passage, supports anode and connects anode to cathode
TCO anode	×	×	light passage, collects electrons
Barrier Coating	×	×	light passage, electron passage, sensitizer surface and prevents charge recombination
Mesoporous Semiconductor Film	×	×	some light scattering, electron passage, sensitizer scaffold and facilitates sensitizer-to-redox charge pair separation
Scattering Layer	×	×	exceptional light scattering and rest same as mesoporous layer
Sensitizer	×	×	absorbs electrons and injects high potential electron into semiconductor
Redox Pair or Hole Conductor	×	×	recycler of electrons from cathode to sensitizer and charge pair separation
Reduction Catalyst	**	×	optimizes exchange of the returning electrons to the recycler
TCO cathode	×	×	collects returning electrons
Transparent Substrate	×		unabsorbed light passage
** Mirror Coating	×		reflects light back into the active cell

TCO abbreviates transparent conductive oxide (typically FTO or ITO). Superscript **mean that the reduction catalyst can also serve as a mirror if a film of Pt coats the cathode's TCO.

In general the optical characteristics of a DSSC depend on the refractive index, structural homogeneity, purity and absorbance of each component. Electrical properties depend on purity, concentration, morphology and arrangement of each part.

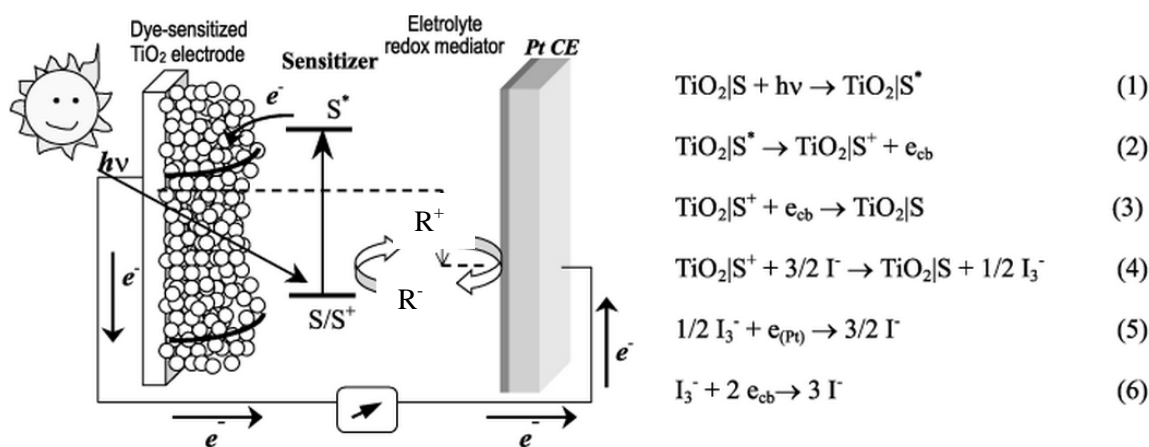
2.3. Guide to Understanding Photovoltaic Mechanisms in a Dye-Sensitized Solar Cell

The essence of photovoltaic action in any PV is photon-induced formation of an exciton followed by the flow of the resultant free electron and hole in opposing directions, current. The free charges meet up and recombine at the PV's cathode after the electron has travelled through an external circuit and performed electrical work; Figure 2-4. The std-DSSC differs from a p-n junction-type PV cell, however, in that the photovoltaic mechanisms are compartmentalized as they are performed in three different DSSC materials. Sensitizer molecules (S) produce excitons upon absorption of certain photon energies (S^*). A wide bandgap SC facilitates the flow of one type of charge carrier through this mesostructured electrode; typically electron transport to the anode. And, a redox couple (R^+/R^-) in an electrolyte solid state or hole conductor allows the flow of the opposite charge carrier to the opposing electrode; typically hole transport to the cathode.

Although three separate materials perform the main light-to-energy, or photovoltaic mechanisms in a DSSC, each material is spatially and functionally integrated because of their intermeshed configuration. Like a chloroplast, proximal integration of functional parts is a necessary consequence of the large adsorption surface area within a small volume afforded by the mesostructured n-SC photoanode. Because they are so intermeshed, it is desirable that each component maximally enhances or at least minimally impedes the performance of the others.

Initially the DSSC can be thought of as a photon-driven electrochemical cell: Figure 2-4. As such, oxidation occurs at the anode and reduction at the cathode. S upon photo-excitation to form S^* and subsequent electron injection into an nc-n-SC particle is oxidized to S^+ at the photoanode. Reduction of the most oxidized redox couple (R^-/R^+) member (R^+) occurs at the cathode (typically TCO + Pt) of the DSSC; R^+ then becomes R^- . However, the DSSC's R^-/R^+ (or hole conductor) recycles electrons between the cathode and S^+ without incurring a net chemical change; none in R^-/R^+ , S^*/S^+ nor at the two electrodes. Thus a salt bridge is not required in this type of electrochemical cell since there is no need for supplemental counter ions. The following

will describe the general processes of charge movement between the two electrodes upon S absorbing an appropriate photon to form S^* .



Reaction 1 is the photo-initiated promotion of a electron to a higher energy level. The forward half-reactions on the right are equations 1, 2, 4 and 5. The counter-productive, recombination reactions are equations 3 and 6.

Figure 2-4: DSSC Photoelectrochemistry. Taken from Ref. 17.

Electrical potential is the force that drives photoexcited electrons to an external circuit where electrical work is performed before returning to the cathode. The potential is usually measured in terms of an electron's energy level in a vacuum, E vs. vacuum level. When outside of its material within a vacuum the potential of an electron is zero. An electron seeks lower E , more negative potential, as it becomes more stabilized (charge stabilized), such as in a chemical bond. The vacuum scale (sometimes called the absolute potential) can easily be converted to an electrochemical potential scale: E° vs. normal hydrogen electrode (NHE) or E° vs. standard calomel electrode (SCE) by the following equations, respectively:

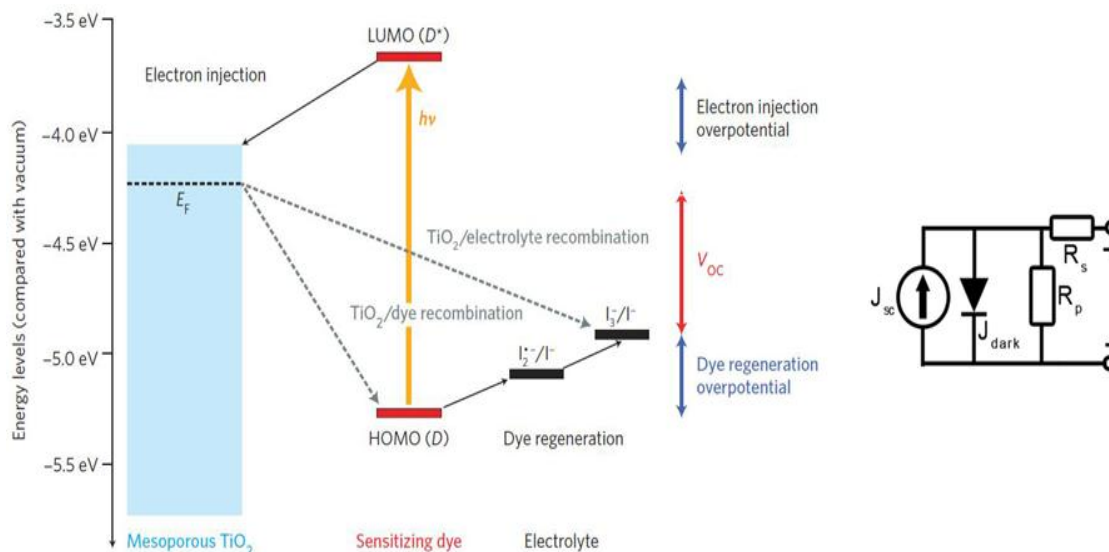
$$E_{\text{VAC}} = E_{\text{NHE}}^\circ + 4.44\text{V} \quad [2]$$

$$E_{\text{VAC}} = E_{\text{SCE}}^\circ + 4.68\text{V} \quad [3]$$

Electrons can be visualized as moving downward (towards a more negative potential) in the vacuum level as physical stabilization occurs within an electrochemical cell; Figure 2-5.

Conversely the hole, which is the absence of a charge, moves upward. As will be discussed in section 2.3.2, when a valence electron in S is promoted by a photon, it moves further from its

parent nucleus or nuclei. Because the promoted electron leaves a less balanced charge state in its stable ground state orbital, an electron-hole pair or exciton is created within the S^* molecule. However, if the electron and hole are not able to move easily into the high density of states (DOS) of the n-type semiconductor's conduction band and the electrolyte, respectively, the exciton will not separate long enough for electrical work to be done. In this case the charges recombine and the energy of the photon captured by S^* will either become a photon again or dissipate as vibrational energy. The bond between the sensitizer and semiconductor is therefore a crucial factor in the electron's transport across this chemical bridge; this process is often called electron injection; further discussion of the SC/S bond can be found in Section 2.6.7.



(a) A std-DSSC energy level diagram shows the V_{OC} to be the difference between semiconductor Fermi level (E_F) and redox potential of hole conducting electrolyte. (b) A simple PV circuit diagram. Notice that high parallel shunt resistance (R_p) prevents charge recombination; a high series resistance (R_s) blocks current from flowing and thereby degrades the cell's fill factor, FF .

Figure 2-5: Electronic Potential Energy Levels of a std-DSSC

As can be seen in Figure 2-5 an electron inside the DSSC reaches its highest electrical potential when in an exciton (sections 2.3.3 and 2.6.7), or lowest unoccupied molecular orbital (LUMO), of the S^* molecule. When the S^* LUMO electron is injected into the n-type semiconductor's conduction band, its potential slightly lowers. In order to reach the external

circuit, the electron must be able to diffuse successfully through the semiconductor's conduction band to the TCO/external contact (sections 2.6.3 and 2.6.4). During diffusion the electron can get stuck in a trap-state or recombine with a hole in S^+ or R^+ .

The most stable energy state achievable by an electron in a sensitizer (S), is when it is localized within a ground state sensitizer's, S's, bonding orbital. After electron injection the S^+ is reduced by R^- (of R^-/R^+ in the electrolyte) to S. Subsequently R^+ must diffuse to the cathode (without recombining with an electron) to be reduced back to R^- by an electron returning from its travel across the external circuit. Additionally, R^- must diffuse to the sensitizers in order to complete its shuttle route between S and the cathode and regenerate S^+ to S again.

Notice in Figure 2-5 that the largest attainable potential created by a DSSC is the V_{oc} . The V_{oc} is roughly the difference between the semiconductor's Fermi level (E_F) and the potential of R^+ of R^-/R^+ (or the valence band of a hole conductor). It can be thought of as the largest difference in potential (difference in charge) that can develop between the external contacts at the cathode and anode of a cell; although some potential drop at the TCO/meso nc-n-SC interface lowers this estimated V_{oc} . However, the further losses in potential across the distance of the cell called overpotentials are accrued in order to achieve thermodynamically favored charge separation and transport.

To summarize, the movement of opposite charges from the exciton to anode and cathode in opposing directions is the DSSC's current; amount of current is initially determined by how many photogenerated excitons are produced during a unit of time. The cell's voltage is the potential difference of the opposite charges upon reaching their respective electrode contacts. Before arriving at opposite electrodes, however, charges typically encounter impediments to their movement. Charges can be ship-wrecked on trap-states or become attracted to the wrong side of the tracks and recombine with an oppositely charged species (called recombination process).

The productive and counter-productive interactions between each of the two charges and other materials and molecules occurring within the cell during charge movement or transport to the electrodes are called charge transport processes or mechanisms. In this section general device physics concepts have mainly been discussed in simple terms; for a more in depth study of device physics applied to a DSSC please read Ref. 18. The speeds, or kinetics, and diffusion lengths of the aforementioned processes discussed were mostly neglected. In the following section photon-to-electron energy transference will be discussed as it is often neglect in DSSC process publications. In Section 2.3 the main mechanisms involved in light-to-energy conversion will described. In Section 2.4 optical performance testing of DSSCs and in Section 2.5 robust DSSC fabrication techniques will be addressed and described such that the sequence of light-to-electrical energy transduction mechanisms performed within a DSSC can be better embraced and utilized for future solar cell investigations. The interrelatedness of DSSC components and the affect it has on exciton production, charge transfer and recombination will be discussed in Section 2.3.3 and 2.3.4 after the following.

2.3.2. Photon-to-Electron Energy Transference

Photovoltaic action begins with the photon transferring its energy to an S molecule's valence electron and forming S^* . For convenience, photon-to-electron energy transference is typically depicted as a photon "colliding" with an atom and subsequently "kicking" one of the atom's valence electrons into a higher energy orbital. The photon bestows its quanta of energy and relativistic momentum to the molecule and then disappears; as is observed using absorption spectroscopy. Upon gaining the photon's energy, an electron is promoted from its ground state orbital to a higher, discrete electronic energy level. After about one nanosecond, on average, the excited state electron returns to its stable ground state energy level by a restorative force and sheds its extra energy by either emitting a photon or activating vibrational modes in the molecule

and surrounding molecules; Figure 2-6. During the former process the emitted photon has energy equal to the difference between the higher and ground state electronic energy levels; as is observed in emission lines or using fluorescence spectroscopy.

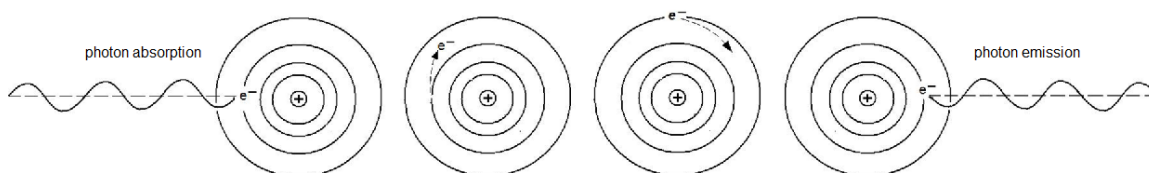
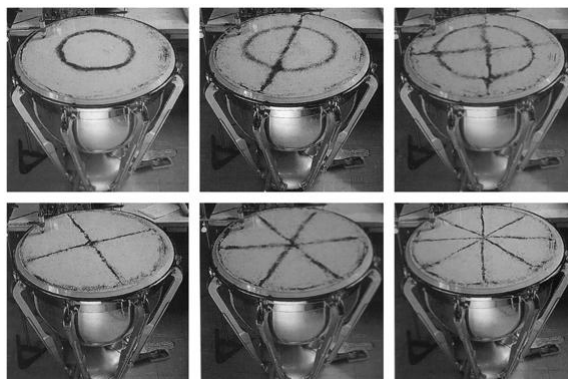


Figure 2-6: Bohr-like Atom Absorbing a Photon's Energy

According to quantum mechanics an electron bound by a nucleus' electric field oscillates distally about it in a three dimensional standing wave. This idea was stimulated by the de Broglie wave theory and later verified by quantum mechanics. The electron's generalized angular momentum is conserved. In fact, it must be discrete so that the centrifugal force on the electron balances the Coulombic attractive force¹ between the electron and nucleus. If not, the electron's change in acceleration (due to its constantly changing direction) would according to classical electromagnetics result in the electron continually radiating a photon, losing kinetic energy and eventually being drawn into the nucleus since the centrifugal force on the electron could no longer counterbalance electron-to-nucleus attraction.

When a photon's energy is absorbed by a valence electron, their electric field oscillation frequencies resonate such that the photon's energy, or momentum, is effectively transferred to the electron's 3-D standing wave oscillations. The electron is then "pushed" into oscillating into a higher energy, allowed 3-D standing wave. Much like a drum skin which oscillates as a 2-D standing wave, only certain standing wave patterns can be made; Figures 2-7(a) and (b).

¹ The potential energy, V_e , of this particle system having a central force (nucleus) can be derived by equating the Coulombic attractive force on an electron to the centrifugal force on that electron circularly orbiting its stationary nucleus: $-kZe^2/r^2 = m_e v_e^2 / r$; where k is Boltzmann's constant, Ze is the charge of the nucleus, r is the distance between electron and nucleus, m_e is the electron's mass and v_e is the electron's velocity.



The patterns above are made by small grains of sand resting on the nodes of the drum skin's allowed standing waves. Note that the outer rim is a node.

Figure 2-7(a): Discrete oscillatory frequencies of 2-D standing waves.

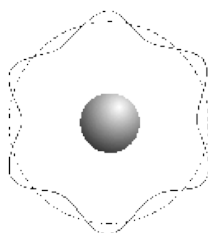


Figure 2-7(b): Depiction of a simple 3-D standing wave.

The concept of discrete 3-D standing wave oscillations explains the absorbance spectra of sensitizer molecules like N719, Black Dye and YD2-*o*-C8; Figures 2-10(a) and (b), Section 2.2.7. Unlike electrons getting promoted across a semiconductor's band gap by a photon whose energy can be much greater than the energy gap, a photon's energy has to be closer to the difference between the highest occupied molecular orbital and the lowest unoccupied molecular orbital energies (HOMO-LUMO energy gap) in order to excite an electron to an allowed higher angular momentum about its nucleus or nuclei. The peaks on the above mentioned spectra show that a certain range of photons maximally resonate with the ground state oscillatory motion of a valence electron.

2.3.3. Charge Transfer and Recombination

As stated above, on average an exciton has a lifetime of about one nanosecond. Such rapid decay necessitates that its two opposing charges be separated within at least the picosecond

timeframe so that useful electrical work can be done. In std-DSSCs interfacial electron transfer from S^* to SC occurs first. S^* 's excited state electron moves very rapidly into the conduction band of the SC where its movement towards the TCO is diffusion controlled (for more information on charge transfer within a DSSC sensitizer see Section 2.2.7); Figure 2-8. Subsequently S^+ is rapidly reduced back to S, its stable ground state, by R^- or a hole conductor. The hole conductor or the electrolyte moves free charge carrier by electron hopping or diffusion respectively, to the cathode. The overall kinetics of charge transfer in a DSSC is diffusion limited by the charge carrier in the electrolyte or hole conductor. Thus, if the diffusion is too slow due to a lack of charge gradient in the electrolyte or anode, for example, the freed electrons and holes will more likely attract and recombine.

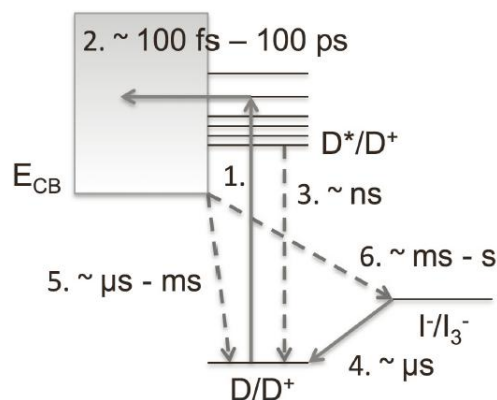


Figure 2-8: Rates of interfacial electron transfer.

Optimally the recombination process at the S^*/S , S^+/S , S^+/SC , S/R^+ , SC/R^+ , or R^+/TCO interfaces should not happen. At the S^*/SC interface desirable electron movement from S^* into the conduction band of a wideband n-type SC is thermodynamically favorable. Enthalpy change is negative because there is a drop in electronic potential from an S^* LUMO to the bottom of the SC's conduction band; Figure 2-5(a). Hole movement away from the oxidized sensitizer (S^+) also results in a negative enthalpy change because there is an increase in reduction potential from the HOMO of S^+ to the redox couple (or hole conductor) at the S/electrolyte interface; Figure 2-5a.

Once in the SC, the electron's movement is predominately diffusion controlled, which means that concentration gradient of electrons throughout the SC mesoporous film drives the electrons toward the TCO. In std-DSSCs there is also a potential drop across the nc-TiO₂/TCO contact. Upon illumination photo-injected electrons in the SC accumulate to form an electric field at this contact, which exerts a force that aids diffusion in pulling electrons across the tumultuous path within the meso nc-n-TiO₂ film.¹⁹ Entropy change for electron and hole movement is positive at S's interface with the SC and electrolyte, respectively. The density of states (DOSs) present in the SC and the redox couple (or hole conductor) for electrons and holes, respectively, are much larger than that in S.

A blocking layer is often deposited onto the TCO film in order to prevent a depletion layer from forming at the TCO/electrolyte or hole layer interface. In turn, the depletion layer would cause band bending at the TCO/nc-n-SC interface, which forms an energy barrier against interfacial electron transfer from the SC to the TCO. The depletion layer would also attract electrons away from diffusing to the outer circuit and towards the TCO/electrolyte interface where they are more likely to recombine with R⁺.

In a std-DSSC a very small electric field at the nc-n-SC/redox couple (or hole conductor) interface forms. The electrical field results from dipole formation (a potential drop) across a Helmholtz layer, which develops within the electrolyte directly contacting the semiconductor in the dark. After initial contact the ncTiO₂ particles are almost completely depleted of majority charge carriers (electrons); due to Debye length, they are not large enough to form a space charge region. Anions within the electrolyte, whose charge is opposite of that induced on the semiconductor's surface, are electrostatically adsorbed onto the surface of the semiconductor. Consequently cations in the electrolyte, whose charge is opposite that of the adsorbed layer, are electrostatically attracted to the adsorbed layer. At this point there is no potential difference at the interface because of the depletion of majority carriers in the SC's conduction band.

But after photogenerated electrons inject into the meso nc-n-SC and sufficiently accumulate the semiconductor's quasi Fermi level (E_F) rises. The resultant potential drop at the Helmholtz layer slightly enhances charge separation; it draws the electron away from the S^* and towards the SC conduction band. At an anatase $TiO_2/[I^-/I_3^-]$ interface there is an estimated 0.3eV drop in potential across the Helmholtz layer.²¹ More importantly, however, the Helmholtz layer significantly acts as a barrier preventing charge recombination at the SC/electrolyte interface. In a std-DSSC the negative charge of the adsorbed anionic layer effectively repels electrons from reaching the SC surface. This barrier helps prevent free electrons in the SC conduction band from reducing triiodide.²⁰

Grain boundaries within and between particles, or the presence of impurities in nc-n-SC particles present trapping problems for electrons. Disconnected molecules at these junctures do not allow free charges to pass without some sort of barrier. If the trapping site is large and concentrated, a large charge can develop and create a dipole moment that can more significantly affect subsequent charge movement in its vicinity.

Notice that each driving force benefitting desirable charge movement costs potential energy. In Figure 2-5 the loss of potential is called overpotential. Reducing overpotential, such as the lowering of the reduction potential of the redox couple for porphyrin sensitizers (Section 2.6.7), can raise the V_{oc} . But in doing so an increase in recombination may occur as the barriers preventing it and/or the drive for desirable charge movement are lowered.

2.3.4. Movement of Light in a DSSC

Because of the intermeshing of DSSC functional materials, light attenuation due to reflection, refraction and scattering by any media must be considered. Use of an anti-reflective coating (ARC) to prevent loss of light reflecting off the front substrate (typically glass) of a DSSC is slightly different from ARCs commonly used for silicon PVs. As discussed in Section 2.6.1 an ARC/380nm cut-off filter, such as Asahi ARKTOP, is used for two purposes: 1) to limit

loss due to reflected light mainly in the 400 to 700nm range, Figure 2-15; and, 2) to limit absorption of light by anatase TiO₂. This quarter wave ARC acts to cancel out reflected waves across the strong absorbance range of N719 dye. The bandgap for anatase TiO₂ is $E_g = 3.20\text{eV} \approx 390\text{nm}$ so most of absorption by the semiconductor (which can impede S^{*}'s charge injection by lowering density of states in the SC) is prevented by the 380nm cut-off filter. The cut-off filter also inhibits triiodide (I₃⁻) from absorbing photons. In std-DSSCs the R⁻ in the R⁻/R⁺ is I₃⁻ solvated in acetonitrile. I₃⁻ has good absorbance of light with wavelengths around 370nm in acetonitrile; when I₃⁻ absorbs light, it can decompose which negatively impacts its electron scavenging role.

On the other hand, the flexibility of the meso nc-n-SC structure presents some interesting possibilities for various light effects aimed at enhancing light harvesting within a DSSC. More discussion on this can be found in Chapter 3.

2.4. Guide to Characterizing the Photovoltaic Performance of Laboratory-Grade DSSCs

Two main light-to-energy efficiency measures are: the incident photon-to-electron conversion efficiency (*IPCE*), also called external quantum efficiency (*EQE*), and the global efficiency, η , or current-voltage characteristic (also called power curve). It is important to learn how to use these tests in order to learn about what is going on inside the cell.

At one end of power curve the current of a cell when there is no resistance in the external circuit and therefore no voltage is measured; this is called the short-circuit current (I_{sc}) or, when divided by the surface area of the cell's active layer, the short-circuit current density (J_{sc}). When there is an infinite amount of resistance in the outer circuit and therefore no current, the voltage of the cell is measured at the other end of the power curve; and this is called the open-circuit voltage (V_{oc}). For each point in between the voltage and current density are measured.

According to Equation 4 below, the global efficiency of a solar cell, η , is dependent upon four performance parameters: 1) V_{oc} ; 2) short-circuit current density (J_{sc} (mA/mm²)); 3) voltage at maximum power output (V_{mp}); and, 4) current density at mp (J_{mp}). The V_{oc} is the maximum voltage achievable by the PV. For a DSSC the V_{oc} is slightly less than the difference between the potential energy level (E_p), Equation 6, of the dye's photo-excited electrons (e^*) and the redox potential of the electron regenerating medium, i.e. R/R^+ ; Figure 2-5(a). And, to a lesser extent, the V_{oc} is contingent on the cell's shunt or parallel resistance (R_p); at an excessively low R_p , separated charges easily recombine thereby lowering the V_{oc} ; Figure 2-5(b).

The J_{sc} is defined as the maximum density of photo-generated electrons flowing through the cell's external circuit per second. In a DSSC the J_{sc} is highly dependent upon the cell's ability to absorb all the light in the solar spectrum under one sun and AM 1.5 conditions, separate excitons, efficiently collect charges, and, to some degree, upon the cell's series resistance (R_s); Figure 2-5(b). The R_s blocks the flow of electrons; this usually is a result of trap states in the nc-n-SC particles or as a result of intra- or inter-nc-n-SC particle grain boundaries. As seen in Equation 5, below, the V_{mp} and J_{mp} strongly impact the FF value; Equation 5. The subscripted mp stands for maximum power point which represents the working power generating condition cell at which $\frac{dJV}{dV} = 0$; Figure 2-9. The FF decreases when the R_{SH} decreases and the R_s increases.

$$\eta = \frac{P_{out}}{P_{in}} \times 100\% = \frac{V_{oc} \times J_{sc} \times FF}{1mW/mm^2} \times 100\% \quad [4]$$

$$FF = \frac{V_{mp} \times J_{mp}}{V_{oc} \times J_{sc}} \quad [5]$$

where P is power; $J = I / A_{cell}$; A_{cell} is active area of PV; FF stands for fill factor

$$E_p = -kZe^2/r^2 \quad [6]$$

where k is Boltzmann's constant; Ze is effective nuclear charge; r is electron shell radius

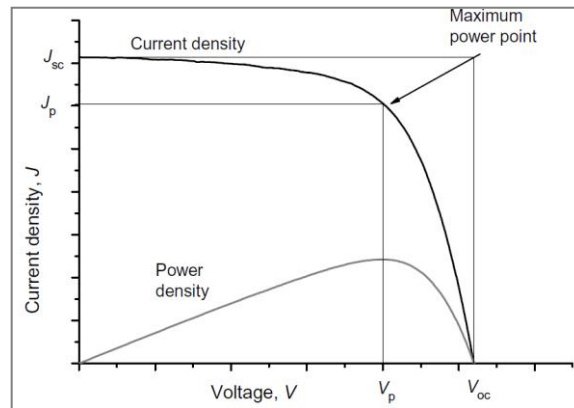


Figure 2-9: Maximum power point of solar cell under illumination.

Notice in Figure 2-9 that the J_{mp} and the V_{mp} are much lower than the current density and potential at short circuit and open circuit conditions, respectively. At maximum power point the current is flowing and so the voltage is affected by recombination, or low shunt resistance. Also at maximum power point the cell is under load and therefore the series resistance in the cell affects the current flow. Thus both J and V drop. In Figure 2-10 it can be seen that the J_{SC} almost equal in both power curves. But the V_{OC} and the efficiency in the upper curve are higher even though its fill factor is lower. The below power curve, as compared to the above, is an example of lower series resistance and lower shunt resistance; Figure 2-5(b).

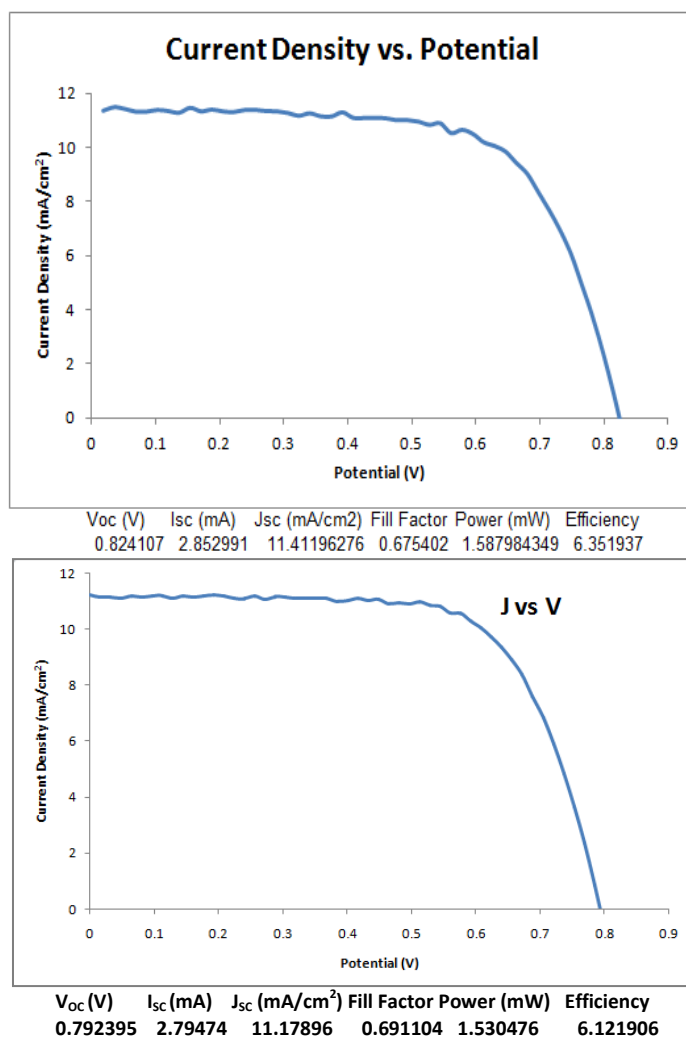


Figure 2-10: Power Curve for DSSC under one sun AM 1.5 conditions.

Essential to analyzing DSSC performance testing is discerning the efficiency function variables and correlating these to physical events occurring within the cell. The *IPCE* is the ratio of the number of collectable photogenerated electrons to the number of incident photons; both quantities are wavelength dependent. A cell's current is measured during exposure to monochromatic light. *IPCE* measurements are particularly useful for quantifying a PV's optical response to spectral irradiance. From it one can trouble shoot various optical problems such as component reflectivity and photoanode connected sensitizer absorbance versus free molecule absorbance; but can also identify the ranges of light where the sensitizer's absorbance has been

enhanced as discussed in Section 2.1. Below are the equations relevant to *IPCE* measurements; subscripts *LH*, *ET* and *CT* stand for light harvesting, electron transport and charge transport respectively.

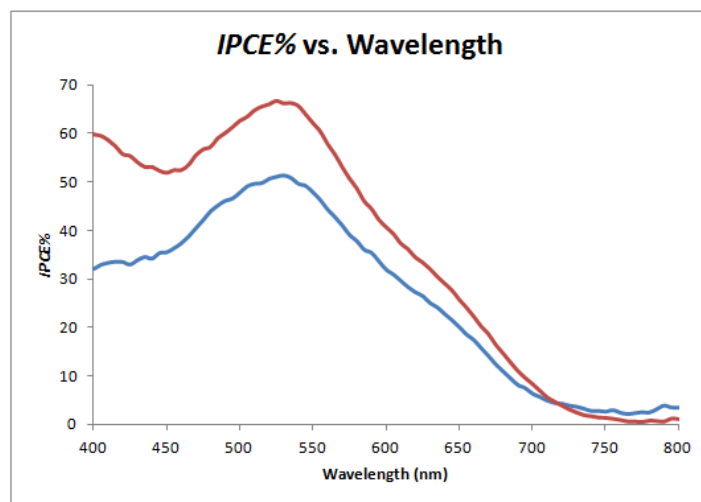
$$IPCE(\lambda) = \frac{\text{number of } e^{-}\text{/sec}}{\text{number of photons/sec}} = \eta_{LH}(\lambda) \eta_{ET}(\lambda) \eta_{CT}(\lambda) \quad [7]$$

$$\eta_{LH}(\lambda) = LHE(\lambda) = 1 - 10^{-abs(\lambda)} \quad [8]$$

$$abs = -\log \frac{I(\lambda)}{I_0(\lambda)} = -1000 \times \varepsilon(\lambda) \times (1/A_{dye}) \quad [9]$$

where *abs* is absorbance; *I* and *I₀* are the intensities of light leaving and incident upon the cell, respectively; $\varepsilon(\lambda)$ is the dye's absorbance at a particular wavelength, *A_{dye}* is the surface area which is sensitized

$$J_{sc} \propto \int LHE(\lambda) d\lambda \quad [10]$$



The *IPCE* values are generated by comparing the DSSC current to a standardized c-Si photoanode. The following equation is used; $\% IPCE(\lambda) = \left[\frac{\{J_{sc\ DSSC}(\lambda) - J_{DK\ DSSC}\}}{\{Area\ DSSC\ (cm^2)\}} \div \frac{\{J_{sc\ Si}(\lambda) - J_{DK\ Si}\}}{\{Area\ Si\ (cm^2)\}} \right] \times 100\%$; where $J_{DK\ DSSC} = 9.6 \times 10^{-7}$ A; $J_{DK\ Si} = 3.99 \times 10^{-7}$ A; Area DSSC = 0.25cm²; and, Area Si = 0.1296cm²

Figure 2-11: Incident photon-to-current conversion efficiency curve for bi-DSSC (red) and DSSC w/o light scattering layer (blue).



Figure 2-12: DSSC without light scattering layer on the right and bi-DSSC on the left.

In the above *IPCE* spectra it can be seen that the spectral response of the DSSC without a light scattering layer is greater over a wider wavelength range than that of the bi-DSSC. The power curves for these two cells are shown in Figures 2-12(a) and (b), respectively. Even though the bi-layer is producing more photogenerated electrons, the R_{SH} of the bi-layer is low and thereby produces less voltage at maximum power; thus its global efficiency is lower. This example demonstrates that spectral response as measured by the *IPCE* is most informative about the cell's light harvesting efficiency. The *J-V* curve, on the other hand, tells more about the cell's charge recombination and series resistance.

To better locate the range of enhanced spectral response by the bi-DSSC versus the DSSC without the light scattering layer, the spectra can be standardized to a value of one; Figure 2-13. Locating the range that is spectrally enhanced by the DSSC modification can truly be identified in the standardized spectra comparison. As will be discussed in Chapter 3, this comparison shows that the photonic crystal's stop band is to the blue side of the standard DSSC peak absorbance. For better enhancement the stop band should be to the red of the sensitizer's peak absorbance as there is more absorbance enhancement to be gained; the slope goes downward further and at a lower absolute value of the slope on the red side than the blue side of the peak.

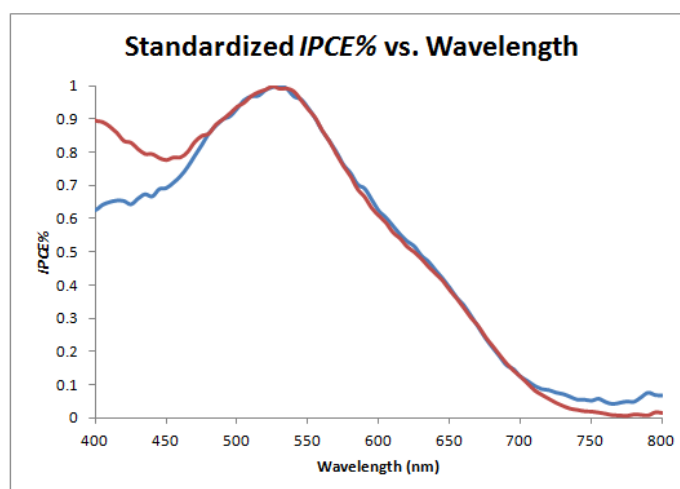


Figure 2-13: Normalized *IPCE* spectra at 535nm for bi-DSSC (red) and DSSC w/o light scattering layer (blue).

In summary, when analyzed properly, there is much to be gained by these simple measurements. The *J-V* curve most clearly provides better information on the efficiency of charge transport than the *IPCE* spectrum. But the *IPCE* spectrum provides more clear information on the light enhancement properties of a modified DSSC, especially when compared to a standard DSSC. In the following section instruction for fabricating standard DSSCs without a light scattering layer will be provided. Following these instructions will facilitate experimental testing of DSSC modification.

Electrical impedance spectroscopy is not discussed here. There are a variety of impedance measuring instruments and programs. But, in general, these measurements can be analyzed to model the cell as a circuit as in Figure 2-5(b).

2.5. Guide to Building Robust Laboratory DSSCs

Initially DSSC fabrication can be thought of as making an anode by connecting a very porous (sponge-like) wide bandgap semiconducting thin film to a highly doped, virtually

transparent electron conductive oxide film supported on a transparent substrate such as glass. The anode is then sensitized and sandwiched to a catalytic Pt cathode using an inert, I/I_3^- resistant spacer that provides a well for the electrolyte just before testing the cell with a solar simulator and Kiethley multimeter. The photoanodes can be prepared well in advance of assembling to the cathode. However, sensitization, the anode-to-cathode connection, and electrolyte infill must be done just prior to testing.

In Figure 2-2 the DSSC without a scatter layer that we consistently fabricate can be seen. The layered components can easily be distinguished. Section 2.5.1 describes the step-by-step process of assembling a std-DSSC. Some components should be prepared in advance. Preparations are described first. Some need to be prepared just prior to DSSC assembly as depicted in Figure 2-2.

Each std-DSSC component can either be purchased or synthesized. Purchasing DSSC components from a reputable dealer is especially worthwhile when time invested in fabricating DSSCs is very limited. On the other hand, synthesizing as many of the components, of course, provides very valuable, intimate experiences with DSSC materials. If it is synthesized, there may be several different synthetic methods described in literature. But only those components which we have tested in functioning DSSCs will be discussed in the following; however, some untested options are described in later sections.

2.5.1. A Step-by-Step Robust DSSC Recipe

In the following, step-by-step procedures for synthesizing and assembling DSSC components into functioning laboratory-grade solar cells are described. In our studies DSSCs were fabricated with a mesoporous $ncTiO_2$ layer having a surface area of 0.25 cm^2 (5 mm x 5 mm) and thickness between 8 to $14\mu\text{m}$. Much effort was made towards developing a consistent methodology so that each cell's performance could be compared to all others produced by these

procedures. By following the below “recipe” carefully, consistency and reproducibility are assured.

With an overall 60% consistency we were able to fabricate lab-grade DSSCs quickly and simply. Our average cell performed light-to-energy conversion $\eta = 6.5\%$ with no effort to optimize their photovoltaic performances. Although the following were not employed in our studies, several procedures have been proven to increase DSSC efficiencies even higher: ²¹ purifying the sensitizer (N719) several times in Sephadex LH-20 column, treating the fabricated photoanode with a sol of 0.04M TiCl_4 (aq) at 70°C for 30 min prior to sensitization, methodical cleaning of all lab equipment with 0.1M HCl in ethanol (to precipitate out Fe^{3+}) just prior to use, utilizing metal-free lab equipment (including oven), vacuum infiltration of electrolyte and using an ARC on the front transparent substrate (a 380 cut-off filter was used during *IPCE* and *J-V* testing, however).

2.5.2. DSSC component preparation

The flow of work for fabricating DSSCs is to build up photoanode, calcine/sinter, sensitize, attach spacer and fill electrolyte. Note that before the final DSSC assembly and subsequent light-to-energy performance testing, the following can be prepared in advance and can remain stable for a minimum of several months:

- 1) Anatase ncTiO_2 particles with an average length of $\sim 25 \pm 10\text{nm}$
- 2) Anatase ncTiO_2 particles with an average length of $\sim 380 \pm 30\text{nm}$
- 3) Pt deposition on FTO coated glass (8 to 15 Ω)... can be cut to size later
- 4) Polymer (cellulose) matrix solution
- 5) ncTiO_2 paste
- 6) Cut anode FTO coated (8 Ω) 1.2mm glass and Pt coated FTO into 1” x 1” squares
- 7) 0.04M TiCl_4 (aq) solution

1) Synthesis of Anatase ncTiO_2 Particles

- a) To prevent contamination (especially by metals), the following glassware should be dedicated to this synthesis. Just prior to nanoparticle synthesis

and subsequent washings of particles, soak glassware in a dedicated base

bath for 12 hour and rinse with copious amounts of DI H₂O :

1. 500mL three-necked round-bottom flask
2. 250 mL round-bottom flask
3. 100.00 mL graduated cylinder
4. 250 mL separation funnel
5. 250 mL beaker
6. Large reflux condenser
7. 1000 or 2000 mL beaker
8. Rotovap trap
9. Low temp and high temp thermometers
10. 30 to 40 mL amber vial
11. Teflon sleeve for Parr hydrothermal bomb
12. Large Teflon stir bar (football shape)

- b) Set up round bottom flask with reflux condenser in an oil bath/heat + stir plate as shown below. Remove flask from bath/heat + stir plate and insert an acetone/dry ice bath. Stabilize acetone at ~ 0°C by carefully adding small chips of dry ice.

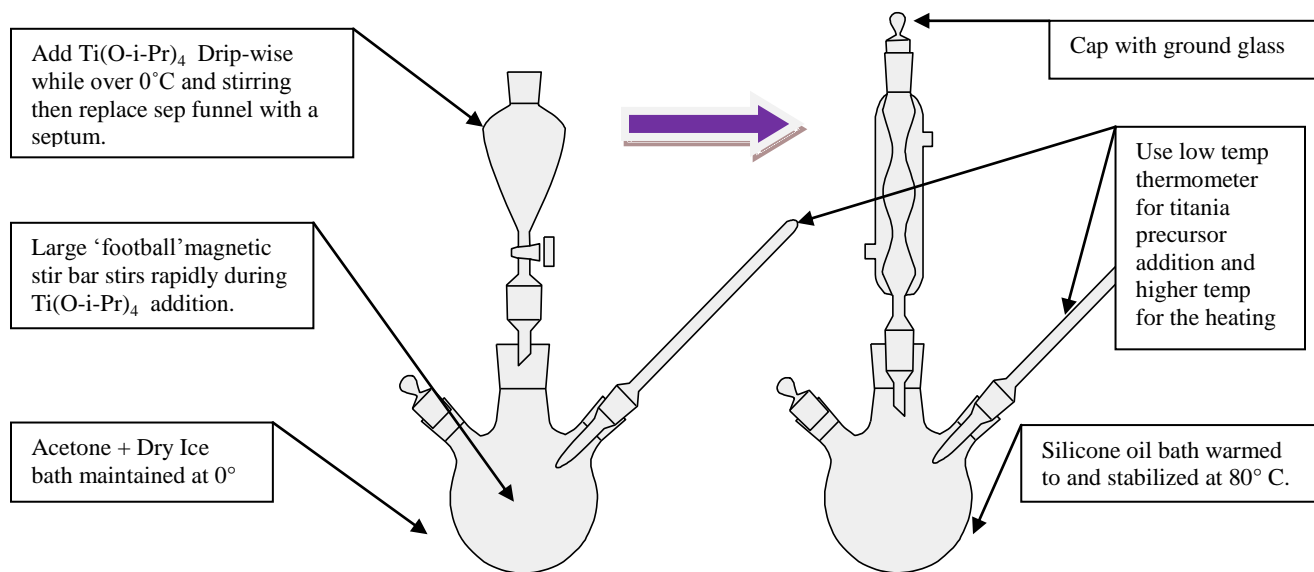


Figure 2-14: Hydrolysis and peptization steps in same round bottom. Attachments and baths are altered.

2) Prepare and stabilize 0°C dry ice and 80°C silicone baths.

- a) Make sure that all glassware is clamped into place in such a way that the baths are interchangeable beneath the round bottom flask.
- b) Fill round bottom flask with nanopure 400mL DI H₂O and 80mL acetic acid, place a large football-shaped stir bar in solution, stir rapidly and maintain equilibration at 0 +/- 2 °C by small additions of dry ice periodically.
- c) Stabilize both baths at the same time; make sure the thermometer in the round bottom flask is in good contact with the rapidly stirring solution. The hydrolysis of titanium isopropoxide in the dry ice bath takes about 45 minutes as does the equilibration of the silicon oil bath.

3) Hydrolyze and peptize titanium alkoxide

- a) In a clean, dry vial (20mL) dispense ~10mL (7.85g) of anhydrous isopropanol using a clean, dry syringe. Note exact weight.
- b) In clean, dry vial (40mL) obtain ~34g of titanium isopropoxide.
- c) Use a clean and dry Pasteur pipette with clean bulb to extract titanium alkoxide from supply bottle. Be sure to keep pipette from touching the sides of the glass as this encourages nucleation of large titania particles.
- d) Tare vial and weigh titania isopropoxide; note exact weight dispensed for use in Step 4k for calculation of TiO₂ produced.
- e) Rapidly pour titanium isopropoxide from vial into separation funnel (drain valve shut) and keep this solution from touching the sides of the glass as much as possible.
- f) Rapidly pour the dry isopropanol into the funnel containing titanium isopropoxide.

- g) Drip wise add the solution in the separation funnel to the rapidly stirring acetic acid solution making sure that the alkoxide is dripping directly into the stirring solution of acetic acid and not onto the glass walls of the round bottom flask. Should take about three-quarters of an hour to add this amount. If additions are not slow large TiO_2 particles will result.
- h) When all titanium isopropoxide solution has been added from separation funnel, remove the empty funnel, and take the round bottom flask out of the ice bath, attach the reflux condenser (with water flowing in it), higher temperature thermometer, and allow equilibration solution to room temperature (25°C).
- i) Once solution reaches room temperature, replace ice bath with pre-heated oil bath and very gradually lower the hydrolyzed titanium solution into the 80°C bath. This should be done over an approximate 45 minute time span.
- j) Place ground glass cap on reflux condenser, make sure solution maintains an 80°C temperature for 8 hours. Swish the solution in the round bottom around occasionally.
- k) Turn off heat and allow peptized sol-gel to continue to stir rapidly while cooling to room temperature. Sol must be at room temperature before proceeding to the next step.

4) Hydrothermal treatment of titanium oxide sol-gel

- a) Make sure that dedicated 100mL Teflon autoclave sleeve is clean and dry and has a mated lid. Prepare the bomb as well.

- b) Measure the total volume of the titanium sol-gel solution; this will be used in conjunction with the amount of $\text{Ti}^{(\text{IV})}$ measured in Step 3d to calculate amount of $\text{Ti}^{(\text{IV})}/\text{mL}$.
- c) In a previously cleaned and dried 100mL graduated cylinder obtain 80mL of the sol-gel.
- d) Place in a previously cleaned and dried 250mL beaker and ultrasonicate for 5 minutes. An ultrasonication bath was found to be superior to a horn sonicator since the tip can more easily contaminate the sol. If using a horn sonicator clean very well by sonicating for 10 minutes in 1:1 acetone and ethanol and then in DI H_2O . Set duty cycle to 50% and power output to 8.
- e) The sol-gel should have a very translucent blue hue to it. If not try sonicating it two or so more minutes. If this color is not apparent the procedure may not have been followed correctly up to this point.
- f) Pour sol-gel into the Teflon sleeve and wipe the mouth before placing the lid on it. Make sure that the lid is machine fitted to the sleeve; if not, the temperature and pressure inside the autoclave will not match what is needed.
- g) Tighten bomb around sleeve and place into a 250°C oven for twelve hours.
- h) Only handle autoclave when it has cooled to room temperature. Open bomb and quickly pour ncTiO_2 solution into a dedicated clean and dry 250mL beaker. Rinse the sleeve into the beaker with no more than 3mL of DI H_2O .
- i) Ultrasonicate the colloidal solution for 5 minutes.

j) **NOTE:** 3 to 4 successive washings of the ncTiO₂ particles in DI H₂O (or ethanol for organic paste) using a centrifuge (10,000 r.p.m.) is recommended so that all TiO₂ precursors and acid surfactant agent is removed; this will open more Ti sites for dye adsorption. However, we did not wash our particles prior to the next steps.

k) Calculate a “12%” ncTiO₂ colloidal solution using the following formula:

“12% wt.” solution as follows:

$$[\text{wt. Ti(O-i-Pr)}_4] / [\text{MW Ti(O-i-Pr)}_4] = \text{mol Ti}^{\text{IV}}$$

$$[\text{mol Ti}^{\text{IV}}] \times [\text{MW TiO}_2 \text{ amorphous crystal}] = \text{wt of TiO}_2 \text{ amorphous crystal}$$

$$[\text{wt of TiO}_2 \text{ amorphous crystal}] / [0.12 \text{ wt/wt}] = \text{wt of “12\% wt” soln total}$$

$$\{[\text{wt of “12\% wt” soln total}] \times [80\text{mL anatase soln}]\} / [\text{total vol. amorphous crystal soln}] = \text{wt of anatase soln}$$

$$[\text{wt of anatase soln}] \sim \text{vol of final anatase soln (after rotovap)}$$

NOTE: Sample calculation for 34g of Ti(O-i-Pr)₄ and 360mL of TiO₂ amorphous crystal soln:

$$\begin{aligned} (34\text{g}) / (284.26\text{g/mol}) &= 0.1196088 \text{ mol} \\ (0.1196088 \text{ mol}) \times (79.866\text{g/mol}) &= 9.552676 \text{ g} \\ (9.552676 \text{ g}) / (0.12\text{g/g}) &= 79.6056\text{g} \\ (79.6056\text{g}) \times (80\text{mL}) / (360\text{mL}) &= 17.69\text{g} \times \text{den water} \approx 17.69\text{mL} \end{aligned}$$

l) Fill a dedicated clean, dry 200mL round bottom flask for the rotovap with the above calculated volume, mark with a permanent marker and pour out water.

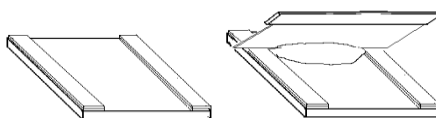
m) Add colloidal solution into round bottom flask and rotovap to the above determined line. **NOTE:** monitor the fifteen to thirty minutes of rotovapping as the solution will tend to bump due to the presence of the isopropanol.

n) Pour colloidal solution into a 30mL amber vial and slowly add one-half the weight of TiO₂ (calculated above) hydroxypropyl cellulose (Sigma Aldrich 435007) while stirring the colloidal solution rapidly. Do not allow to clump.

- o) Allow solution to stir rapidly and ripen for two days. Then stir very slowly, so that air bubbles do not form, but constantly until paste is used.
- p) We have observed that the proper consistency of the aqueous paste is as follows: dip a clean, dry glass rod into the fully ripened paste; it should fully stick to the rod but have a non-viscous texture.
- q) **NOTE:** If making organic paste, use prepared solutions of ethyl cellulose discussed in Ref. 23. Then rotovap paste to a mayonnaise-like texture. The organic paste does not have to be continually stirred after ripening.

5) Photoanode assembly

- a) Clean and make FTO coating hydrophilic immediately before applying paste using the doctor blade method as shown below. Sonicate pre-cut (1" x 1") FTO pieces in one drop of hand soap per 60mL of DI H₂O for 20 minutes. Rinse thoroughly in DI H₂O and sonicate FTO in 1:1 acetone and ethanol solution for 20 minutes. Rinse thoroughly in DI H₂O and sonicate in DI H₂O for 30 minutes.



- b) Dry a few FTO pieces using a low pressure stream of N₂
- c) Use 2 to 4 layers of scotch tape for screed guides on cleaned FTO as shown above.

- d) Drop an ample amount of ncTiO_2 paste onto FTO, use a plastic razor and screed the supply of paste once holding blade at a 45° angle. Be sure to wipe blade between screeds.
- e) Immediately place FTO with paste under a clean bowl and allow paste to level and relax for about 10 minutes each.
- f) Place relaxed films in air but cover loosely with Al foil so that dust does not contaminate drying films.
- g) Allow to fully dry before removing scotch tape.
- h) Calcine and sinter meso ncTiO_2 films in a dedicated oven so that metal contamination does not occur. Ramp temperature to 450°C at a rate of 5°C per minute. Dwell at this temperature for thirty minutes and allow to cool slowly (no faster than 10°C per minute).
- i) If sensitizing films immediately, allow meso film to cool to 160°C , carefully remove hot film with heat resistant plastic or ceramic tweezers and very slowly dunk into a 0.4mM N719 dye in 1:1 acetonitrile and *tert*-butanol solution that was prepared just before sensitization. To mix well, sonicate for 30 minutes.
 - a. Prepare 40mL of a 50/50 volume: acetonitrile/*tert*-butanol solution in a dark amber vial.
 - b. Using micro-spatula weigh out 0.0075 to 0.0090 g of N719 powder (it is stored in Anna's second drawer from the top- it is available at Solaronix under the name Ru 535-bis TBA).
 - c. Add the N719 dye powder to 50/50 in dark amber vial, cap, parafilm cap and sonicate for 30 min.
- j) Leave films completely immersed in dye in the dark for 48 hours before removal and rinsing gently in acetonitrile.

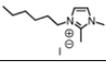
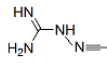
- k) **NOTE:** If not sensitizing immediately, place these cooled films in a dry, dark container for later sensitization. Must heat film to 300°C before cooling to 160°C and dunking films.
- l) After rinsing and drying dyed films for about 10 minutes, immediately scrape off film only leaving a 5mm x 5mm area of dyed film; see Figure 2-11. Do not scrape film off using the plastic razor blade like a chisel. Instead, hold razor approximately perpendicular to the FTO surface and 45° to the edge you are leaving behind. If dragging the blade down towards you, the edge of the blade closest to the edge you are leaving is the furthest away from you. **NOTE:** If you do this incorrectly, the dyed meso film will separate from the FTO and the film will not have an ohmic contact with the FTO; hence the V_{oc} and the FF will be noticeably low.

6) Assembling DSSC for testing.

- a) Immediately after scraping away excess dyed film, carefully wipe the FTO with an acetonitrile dampened lint-free napkin.
- b) Cut out a ~4" x 4" piece of parafilm and stretch it evenly to almost twice its original area using your index finger and thumb on both hands as though they are large, flat clamps.
- c) While just stretched, place parafilm over FTO/dyed film and press gently the parafilm into the FTO and rub many times with your thumbs to warm it up so the parafilm sticks to the FTO. Do not wrinkle the parafilm since it acts as a flat spacer between the anode and cathode and a well for the electrolyte.

- d) Cut a window out of the parafilm using a sharp ceramic razor such that you the parafilm window is about a half a millimeter or so beyond the dyed meso film. Do not cut into the dyed film as it will cause meso/FTO separation.
- e) Using fresh, sonicated electrolyte according the recipe below, drop one drop of electrolyte into the parafilm well using a Pasteur pipette. The electrolyte should have a meniscus that barely stands above the top of the parafilm.

Table 2-2. Materials list for 5mL of I⁻/I₃⁻ electrolyte

Material List for 5 mL of Iodide/Triiodide Electrolyte								
Compound	CAS No.	Structure	Source and Product No.	Location in Lab	Quantity	mol/L in the 5 mL soln	MW(g/mol)	den(g/cm ³)
I ₂	7553-56-2		99.99% pure		63 mg	0.05		
Lil	10377-51-2		99.9% pure		170 mg	0.1		
3-hexyl-1,2-dimethylimidazolium iodide			Solaronix: DMHII		0.927 g	0.6	309.1	
4-tert-butylpyridine			99% pure		0.338 g	0.5	135.21	0.923
Guanidium isothiocyanate	593-84-0		97% pure		59 mg	0.1	116.14	
Acetonitrile	75-05-8		99.8% pure		5 mL			

Procedure:

- a. With a 10mL syringe extract anhydrous acetonitrile from container and dispense into a 20mL vial.
 - b. Add the pre-weighed dry compounds (see materials list above) to the acetonitrile.
 - c. Cap vial and seal cap with parafilm.
 - d. Sonicate the solution for 30 minutes.
- f) Immediately place the pre-prepared platinized Pt cathode (procedure below) on top of parafilm spacer. Hold firmly together (do not squeeze, however) while attaching two binder clips onto the sandwich of electrodes. It is important that you leave about one-quarter of an inch of

each electrode protruding out in opposite directions to that alligator clips may be easily attached for solar simulation measurements.

1. Coat 8 to 15Ω FTO coated glass sheets (6" x 6") with a 5 nm thick layer of Cr and a 100 to 150 nm thick layer of Pt using sputter or evaporative deposition.
2. Preparation of the 5mM solution of hexachloroplatinic acid:
 - **The Math:** (0.010 L solution) \times (0.005 mol H₂PtCl₆ / L soln) \times (1 mol H₂PtCl₆•H₂O / 1 mol H₂PtCl₆) \times (517.903 g / mol of H₂PtCl₆•H₂O)
 - Materials list:

Material list for 5mM of hexachloroplatinic acid						
Compound	CAS No.	Source and Product No.	Location in Lab	Quantity	MW(g/mol)	den(g/cm ³)
H ₂ PtCl ₆ •6H ₂ O	16941-12-1			26 mg	517.903	2.431
Dry Anhydrous 2-propanol	67-63-0		under Anna's sink	10 mL	60.1	0.786

Procedure for preparing the hexachloroplatinic acid:

- a. Place a 20mL vial in 100°C oven overnight to dry from moisture.
- b. Draw out 10mL of 2-propanol with a syringe and have ready while weighing out the hexachloroplatinic acid.
- c. Tare the vial and leave the vial close to scale while weighing out the hexachloroplatinic acid powder.
- d. Weigh ~26mg of the hexachloroplatinic acid and immediately place the acid into the tared vial and add 10mL of dry anhydrous 2-propanol.
- e. Solution should be yellow.

Procedure for coating the Pt with hexachloroplatinic acid:

- a. Coating the Cr/Pt metal with hexachloroplatinic acid:
 - Place the metal coated glass plates (1"x1") in the oven, ramp heat to 405°C @ 5°C/min, dwell at this temperature for 15 minutes and ramp heat to 30°C @ 10°C/min.
 - With a pipet evenly and fully wet the surface of the metal coating with the hexachloroplatinic acid solution.
 - While 2-propanol is evaporating, swirl plate in the air in a Figure eight pattern to evenly disperse liquid on the surface as it dries. Hold the plate with tweezers.
 - **Note:** if dark spots form on the Pt surface upon drying, syringe filter the hexachloroplatinic acid solution to remove precipitates.
- b. Store the remaining hexachloroplatinic acid in a dark drawer.
- c. When the Power Curve goes down, dispose of the cathode and re-coat a new one.

2.6. Detailed Descriptions of DSSC Components

2.6.1. Anti-Reflective Coating

Incoming light first encounters the ARC, which is designed to suppress reflection of visible range light waves at the ambient medium-substrate interface of the DSSC; Figure 2-2. The ambient medium and substrate are typically air, with a refractive index $n_{\text{amb}} = 1.0$, and glass, with $n_{\text{sub}} = 1.56$, respectively. A single-layer quarter-wave AR coating enhances the transmission of light incident on the substrate by causing destructive interference between light reflecting off of the ambient medium-AR coating interface and light reflecting from the AR coating-substrate interface. The wavelength of light whose reflection is maximally suppressed, or minimally reflected, π_{min} , by the AR coating is represented in the equation below.

$$\pi_{\text{min}} = 4n_c d \quad [1]$$

where n_c is the geometric mean of ambient and substrate media refractive indices, $(n_{\text{amb}}n_{\text{sub}})^{1/2}$

and, d is coating thickness

Preferably π_{min} lies in the middle of the spectrum of light absorbable by the specific DSSC sensitizer. For example, the π_{min} for di-tetrabutylammonium cis-bis(isothiocyanato) bis(2,2'-bipyridyl-4,4'-dicarboxylato) ruthenium(II), or N719 dye, would be 535nm. On the other hand tris-tetrabutylammonium tris(isothiocyanato) (2,2':6,6''-terpyridyl-4,4'4''-tricarboxylato) ruthenium(II), or Black-dye, would use $\pi_{\text{min}} = 610\text{nm}$; Figures 2-9, 2-10(a). A more detailed analysis of Fresnel reflectance over a range of incident angles can be carried out using the Fresnel equations for s- and p-polarized light.

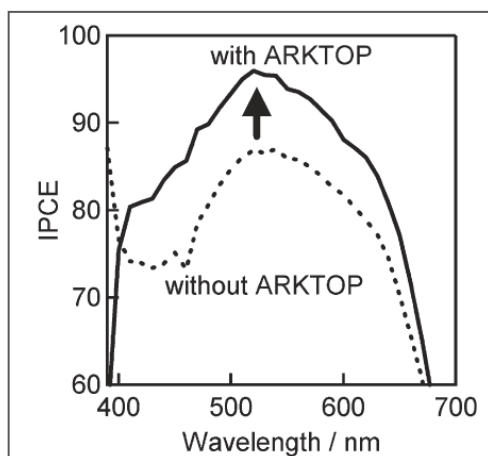


Figure 2-15: IPCE spectra of an N719 dyed std-DSSC with (solid line) and without (dashed line) Asahi's ARKTOP 380nm cut-off filter/AR coating.

Asahi manufactures a self-adhesive fluorinated polymer AR coating called ARKTOP. It is a combination UV cut-off filter (at 380nm) and AR film; 380nm corresponds to the bandgap of anatase TiO_2 . As seen in Figure 2-15, by allowing 10% more photons to pass through the surfaces of the cell's front substrate, the AR film increases the light harvesting ability of a DSSC.

Alternatively a silica bead sol-gel can be spin-coated onto the glass or polymer substrate to form an effective AR coating

2.6.2. Front Substrate

The front substrate serves four purposes: 1) transmits light; 2) protects the active parts of the cell; 3) a rigid surface for sealing Surlyn gasket (see Figure 2-2); 4) supports TCO deposited film. 1) Allowing light to pass through it is one of its main functions; to help it perform this it is important to keep its surfaces clean and free of scratches. 2) Oxygen in the air is an excited state quencher for some dyes. 4) Typically glass is used as a substrate since it facilitates chemical vapor deposition (CVD) of a TCO film, i.e. fluorine-doped tin oxide (FTO), on one of its faces. There are low temperature TCO film procedures for plastics, which will not be discussed here.

2.6.3. Transparent Conductive Oxide Layer: Photoanode

The TCO film serves to transmit light and act as an ohmic contact for the photoanode. A ~600nm TCO film is typically deposited by CVD, evaporation or sputtering onto glass. TCOs are usually heavily doped p-type semiconductor films with wide band gaps. FTO and indium tin oxide (ITO) films are common TCOs for optoelectronic devices. Photogenerated current is better extracted from the TCO when a highly conductive metal bus bar is connected to the FTO film. This can be a low-viscosity silver epoxy, an adhesive foil tape (i.e. tin-plated copper) or Cerosolza solder.

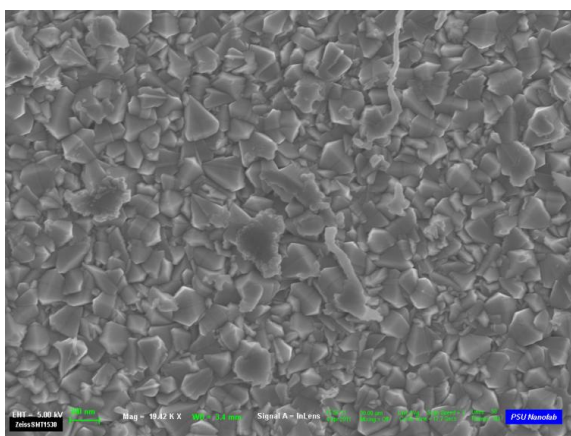


Figure 2-16: SEM image of the top of a FTO film deposited on glass.

The resistivity, ρ , of the TCO is the inverse of its conductivity, σ . The optical transparency of the film decreases with decreasing ρ ; thus, for example, a $4.8 \times 10^{-4} \Omega \cdot \text{cm}$ film is less transparent but more conductive than a $9 \times 10^{-4} \Omega \cdot \text{cm}$ film. Although it is very expensive (indium's naturally occurrence in the earth's crust is very low), an ITO film can have very desirable characteristics for solar cells: high optical transmittance (>80%) and a low resistivity $\sim 10^{-4} \Omega \cdot \text{cm}$. For some TCOs, however, a balance between transparency and conductivity must be addressed. The optical transmittance spectrum for FTO is presented in Figure 2-17. It can be seen that FTO's optical transmittance permits most light waves beyond about 370nm; but with some attenuation.

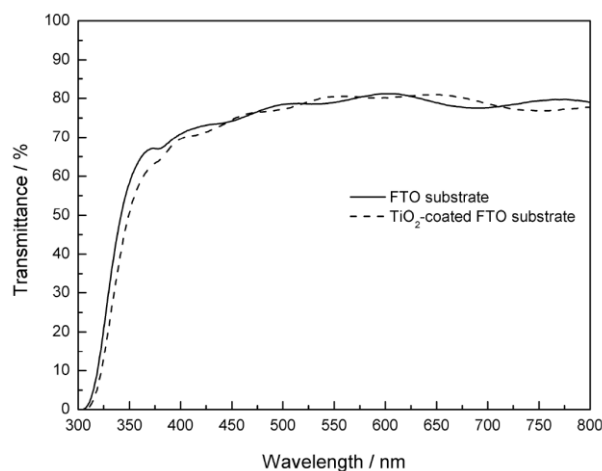


Figure 2-17: Transmittance spectra of FTO with and without a TiO₂ barrier layer.

2.6.4. Barrier Layer

The barrier layer is a thin film, typically ~40nm, of a continuous polycrystalline semiconductor film (same material used in mesoporous layer) deposited onto the TCO film. Its most commonly cited function is to block electrons from diffusing through the TCO layer and recombining with the oxidized ion of the redox couple. By preventing recombination, the barrier layer suppresses dark current and current loss at the FTO/redox pair interface. But the blocking layer has another very important role that should not be overlooked. It must provide good electrical connectivity between the mesoporous and the TCO layers. When the mesoporous layer is not well connected to the FTO (via the blocking layer), as in Figure 2-18a, sheet or series resistance at the anode develops. Methods for improving the anchoring character of this layer have been investigated via electrodepositing the sol.²² However, spin-coating a sol-gel is a much easier method of coating the TCO; Figure 2-18(b).

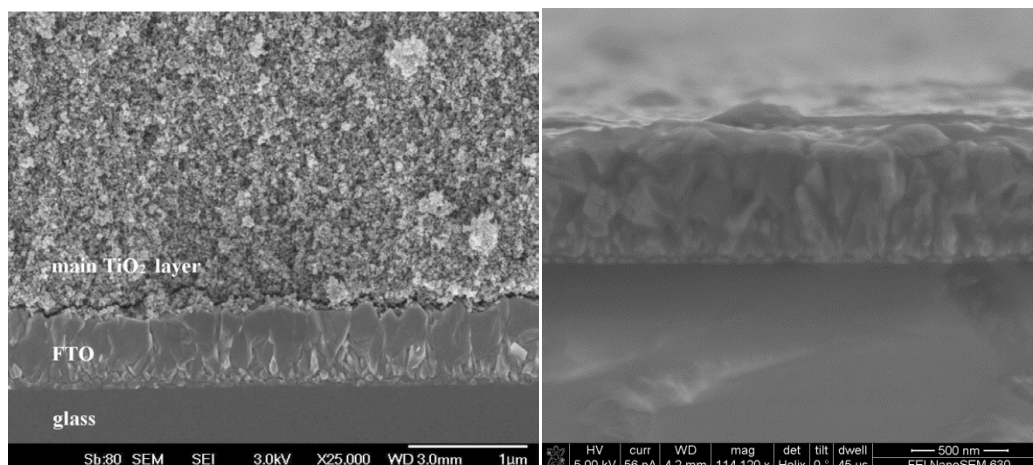


Figure 2-18: FESEM image of meso-ncTiO₂/ blocking layer interface and barrier layer on FTO.

This layer's crystal morphology is an important characteristic for determining conductivity of the blocking layer. The larger the crystal size in this layer, the more conductive is the barrier layer. Increasing crystal size generally results from longer calcination dwell times.²³ Nonetheless, thinness of the blocking layer is very important since anatase TiO₂ has a high refractive index ($n = 2.488$) and a narrow enough

2.6.5. Mesoporous Layer of Sintered Semi-Conductor Nanoparticles

The mesoporous nanocrystalline n-type semiconductor layer (meso nc-n-SC) is a salient DSSC structural feature. The film resembles a sintered frit; Figure 2-19. Its main function is to provide a large specific surface area for maximal dye loading. In other words, the meso nc-n-SC layer should accommodate a maximal amount of attached dye molecules (typically by adsorption) within a minimal depth of film. To enhance surface area (for greater dye loading) as well as reduce necking at nc-n-SC to nc-n-SC particle connections the sintered meso nc-n-SC film is treated with a strongly acid sol.

The meso film must also accept electrons, which are generated at the least negative (vacuum scale) potential of the sensitizer excited state, from the sensitizer molecules and allow them to migrate effectively to the TCO. The electrons diffuse through the n-type semiconductor

whose band gap is wide, 3.2 eV for TiO_2 , and whose conduction band is aligned both the TCO's Fermi level and the excited state electronic level of the sensitizer.

Moreover it must allow the redox pair (or hole conductor) to completely infuse its voids in order to make continuous contact between the redox couple (or hole conductor), the sensitizer and the cathode; this facilitates less-resistive electron recycling between the cathode and sensitizer: Figure 2-4. The typical DSSC employs a $\sim 14\mu\text{m}$ thick meso nc- TiO_2 film so that the timescale of electron diffusion to the TCO layer is short relative to the timescale of recombination at the nc-n-SC surface; Figure 2-8. However, thicker active layers have been investigated.

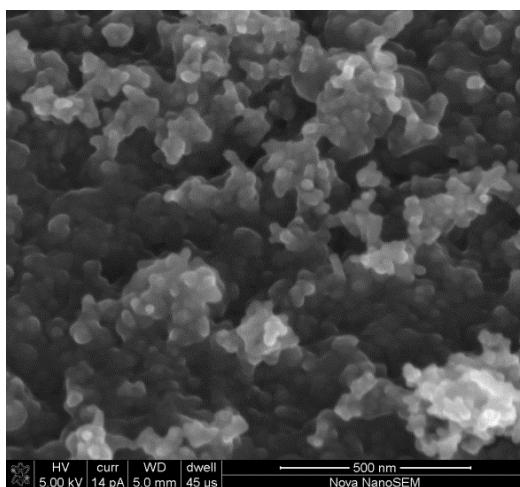


Figure 2-19: SEM cross-sectional image of mesoporous nc-n- TiO_2 film after focused ion beam trenching.

The size and morphology of the nc-SC particles are significant. The optimum nc TiO_2 particle size has been determined to be 20nm. The optimal morphology for nc- TiO_2 particles is anatase truncated octahedral; this shape can be seen in the two darkly silhouetted TiO_2 nanocrystals located near the center of Figure 2-20. The majority of exposed surface on this type of nc- TiO_2 particle is the $\{101\}$ facets. However at the cut off ends of the crystal are small areas of $\{001\}$ facets which are known to increase the meso nc- TiO_2 performance; perhaps due to higher surface energy.

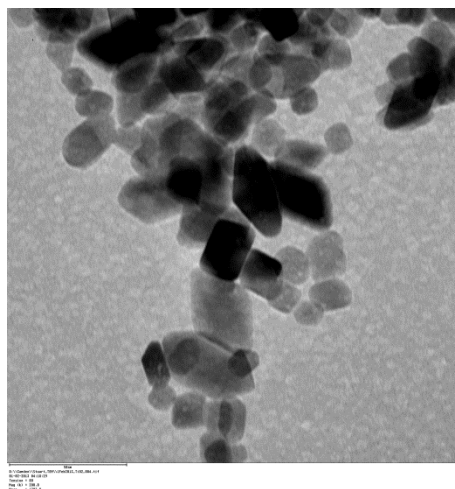


Figure 2-20: TEM image of TiO₂ nanocrystalline particles. Scale bar, bottom left, is 50nm.

2.6.6. Light Scattering Layer

Fused to the back of a std-DSSC's meso nc-n-SC layer is a mesoporous sub-micrometer nanocrystalline SC (meso μ c-SC) layer. This layer induces Mie scattering of the incoming light waves which have transmitted through the meso nc-n-SC layer; Figure 2-3. Upon scattering the light's passage through the cell is extended and the sensitizer's absorbance is increased. But this light-trapping effect comes with a cost. The meso μ c-n-SC layer has a lower surface-to-volume ratio than the meso nc-n-SC layer; thus fewer sensitizer molecules per unit volume are accommodated.

Made of the same semiconductor material as the nc-n-SC particles, the μ c-n-SC particles are usually ~400 to 800 nm. The μ c-n-SC particle size in this layer determines which range of visible light is predominately scattered; the larger the size, the larger the wavelength scattered. The scattering particles take form by consecutively layering sol-gel. Several hydrothermal treatments of seed nc-n-SC particles in the metal oxide sol-gel are required to produce useful sizes of μ c-n-SC particles. The thickness of the meso μ c-n-SC layer is typically between 2 to 5 μ m so that maximum light scattering occurs without too much loss of sensitizer surface area.

2.6.7. Sensitizer Monolayer

Adsorbed onto both meso and macro SC layers, as described above, each sensitizer molecule must anchor to the SC's surface, absorb light and inject electrons into the SC's conduction band. The sensitizer molecules are the key to the photovoltaic effect being initiated. The DSSC's V_{oc} and J_{sc} hinges on the sensitizer's photochemical and photophysical characteristics. The V_{oc} is determined by first measuring the change in potential between S and S^* . The photoexcited electron of S^* must have a high enough overpotential to be injected into the SC's conduction band; Figure 2-5a. And, since the dye regeneration overpotential is determined by the redox pair's potential, and each sensitizer is matched to a specific redox pair, the V_{oc} can be increased by using an electron regeneration pair with a low redox potential; Figure 2-5a. Porphyrin dyes for example are matches with a $Co^{(II/III)}$ complex; resultantly the V_{oc} is 935mV compared to I^-/I_3^- electron regeneration pair (matched with N719 dye) which yields a V_{oc} of ~750 to 800mV. The sensitizer's light absorbance and absorption range must also be high and broad, respectively, so that each incident photon's probability of being absorbed is raised and so that more of the sun's available power is utilized, respectively; Figures 2-22(a) and (b).

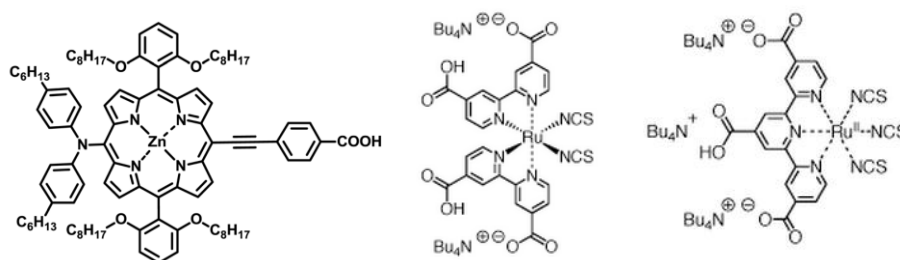
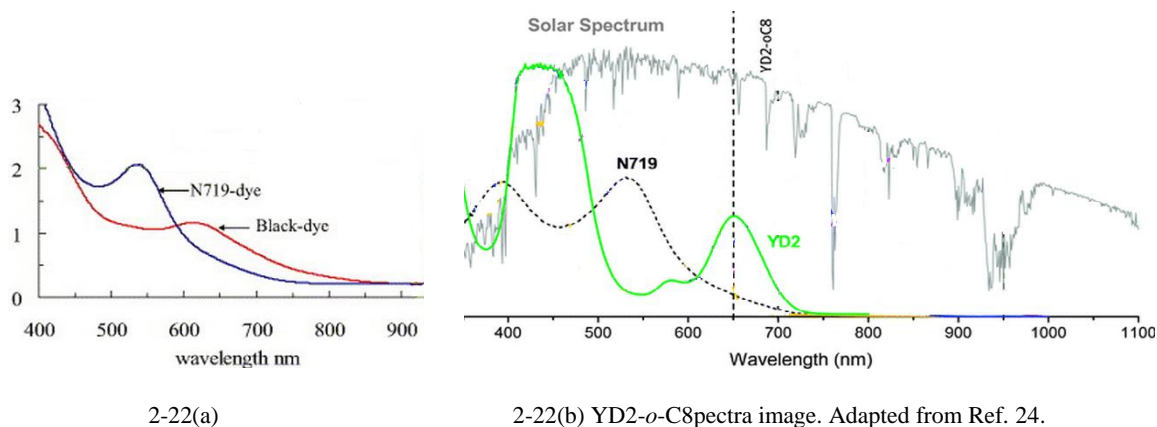


Figure 2-21: High Performance DSSC Sensitizers; YD2-*o*-C8, N719 and Black-Dye.

The anchoring and electron injection characteristics of a sensitizer molecule are somewhat interrelated. The carboxylate moiety on the 4,4' or 4,4',4''-positions of the polypyridyl ligand is used to anchor ruthenium sensitizers onto the metal oxide p-type SC. The carboxylate moiety also aids in injecting the excited state electron into the nc-n-SC. Ordinarily one of the

carboxylates attaches both its oxygens to high surface energy titanium atom by donating unbound valence electron pairs to form a bidentate-bridging bond; the other carboxylate forms an H-bond with a hydroxyl terminated titanium atom. The carboxylate's strong electronegativity pulls the delocalized, high potential electron towards itself. Subsequently, due to the carboxylate's π -bonding nature with the titania, the electron moves swiftly into the high density of states present in the SC's conduction band.

Before arriving at the carboxylate group, however, the delocalized excited state electron in the ring structure must have incentive to leave. For N719 and Black dyes each carboxylate substituent is bonded to the polypyridyl ligand's carbon atom with the highest electron localization (4,4' or 4,4',4''-positions). Conversely, all of the four functionalized carbons of the YD2-*o*-C8's porphyrin ring have the same electron density. So, a donor- π -acceptor configuration is exploited in order to more effectively draw the delocalized, excited-state electron away from the porphyrin ring and towards the anchoring, electronegative carboxylate; Figure 2-21.



2-22(a)

2-22(b) YD2-*o*-C8 spectra image. Adapted from Ref. 24.

Figure 2-22: Sensitizers' Absorption Spectra; N719, Black-Dye and YD2-*o*-C8.

Sensitizers must also be able to accept electrons from the redox pair or hole conducting material. Therefore the sensitizer and redox pair material are typically matched. As mentioned, the recently developed porphyrin dye, YD2-*o*-C8, is regenerated by a $\text{Co}^{(II/III)}$ -bipyridyl complex; Figure 2-21.

Additionally the sensitizer molecules must not agglomerate upon adsorbing onto the SC surface. Agglomeration caused reductive quenching by the surrounding, un-anchored sensitizer molecules. During quenching, the high potential electron relaxes to a lower energy state before it can be injected into the metal oxide's conduction band. Black dye is a good example of a sensitizer that requires a co-adsorbent in order to prevent counterproductive clustering.

Chapter 3. Coupling an Inverse Opal to a Mesoporous Semiconductor Layer

3.1. Overview of Photonic Crystal Coupled DSSCs

Coupling a three dimensional photonic crystal (3D-PC) to a meso nc-n-SC layer forms a composite photoanode capable of harvesting unique ranges of light. The optical properties of the bi-DSSC significantly deviate from those of its separate constituents: a 3D-PC photoanode and a meso nc-SC photoanode; Figures 3-2a and b, respectively. Investigating the nature of light's interactions with a bi-DSSC is of interest due to its complexity and distinctiveness. For example, more detailed information about light wave interactions occurring specifically at the 3D-PC/meso nc-n-SC interface is sparse.

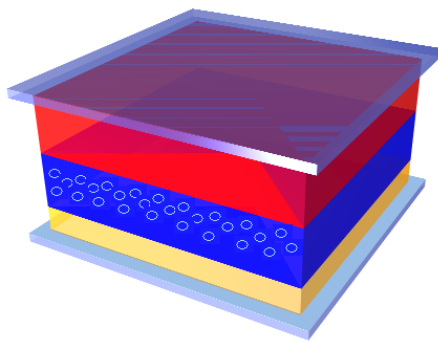


Figure 3-1: 3D photonic crystal coupled DSSC

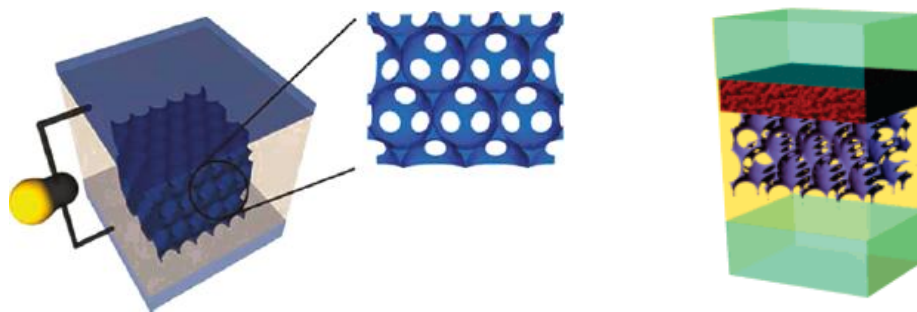
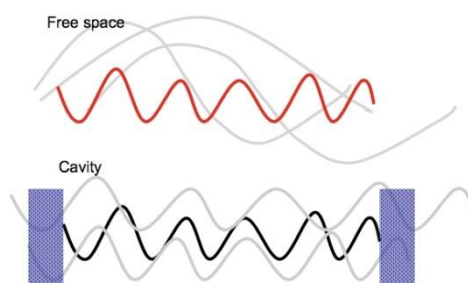


Figure 3-2: Illustrations of 3D-PC DSSC and bi-DSSC. Taken from Refs 25 and 26.

As discussed in section 1.3, superposition of these two photoanodes' global efficiencies has not been realized in a bi-DSSC. Of course, superposition is unattainable since the spectrum of light incident on the dyed 3D-PC layer in a bi-DSSC, after passing through the dyed meso layer, is very different from that impinging on a 3D-PC DSSC; much of the light in the 450 to 650nm range does not make it to the 3D-PC layer as it is efficiently absorbed by the meso layer. In fact, comparing the light-to-energy performance of a 3D-PC DSSC and a bi-DSSC presents a problem. The stop bands for efficient 3D-PC DSSCs and bi-DSSCs are typically quite different. In the 3D-PC DSSC the stop band is larger than the absorbable light by the sensitizer. For example the distance between the scatter centers is typically about $1\mu\text{m}$ for a 3D-PC DSSC and about 300 to 500nm for a bi-DSSC.

After back-reflecting, the meso nc-n-SC layer can act as a cavity resonator; Figure 3-3. However, detailed empirical evidence of this occurring in a bi-DSSC is absent. A possible destructive effect is Wood's anomalies. This effect has to the best of my knowledge only been explored in 3D-PCs. The 3D-PC's surface layer can act as a diffraction grating. In doing so, slow photon resonant modes can be siphoned away since light waves entering the 3D-PC having the correct frequencies are not available for interference.



Note: The black colored wave resonates within the cavity. The wave pattern is trapped as a standing wave between the dielectrics.

Figure 3-3: Resonant wave guiding in a cavity causes light localization.

Alternatively, the lack of superposition of these photoanodes' efficiencies could be due to the lack of achievable connectivity between the two in a bi-DSSC. Slow photon propagation inside the 3D-PC which has been observed to enhance the performances of a bilayer photocatalysts and quantum dot decorated 3D-PC DSSCs may not translate into photocurrent gains in a disconnected bi-DSSC. A bi-DSSC which does exhibit good connectivity according to the electrochemical impedance spectroscopy (EIS) measurements reported, managed a respectable $\eta = 8.6\%$; still, a disconnected bi-DSSC has been reported to perform at $\eta = 8.3\%$. But when a 3D-PC DSSC is able to perform at $\eta = 4.6\%$ and a scatter layer-less DSSC at $\eta \geq 6.6\%$, there exists much room for realizing superposition of efficiency performance in a bi-DSSC.

Closer analysis of the superposition of these two DSSCs' performances is a therefore a worthy investigation. It would be an appropriate primer to further studies of light effects at the 3D-PC /meso nc-n-SC interface and cavity resonances. In the following section the basics of diffraction and slow light propagation inside a 3D-PC will be described. In the sections that follow that will be a description of bi-DSSC design strategies, experimental bi-DSSC material choices, experimental bi-DSSC fabrication and conclusions.

3.2. How a Photonic Crystal Guides Light Waves

A photonic crystal (PC) is a three dimensionally periodic, mesoscopic array of light scattering centers. Light waves exhibiting strong interactions with a particular PC have wavelengths comparable to its lattice parameter, p . Characteristic properties of propagating light, x-ray and electron waves inside their respective periodic crystals share one fundamental mechanism: *interference* of scattered waves. In fact, electronic band gaps in semiconductors and photonic band gaps (PBGs) in PCs form because of wave diffraction at Bragg planes. Analogous to solid semiconductor materials, the density of states for light frequencies within a 3D-PC's PBG are zero or low; their propagation inside the 3D-PC is thereby forbidden. Resultantly, the light consecutively diffracted by a specific in-plane periodicity intensely back-reflects forbidden light waves. The iridescence of light consecutively diffracted by the in-plane (111) periodicity into the (111) specular reflection direction stands as a good example; Figure 3-4.

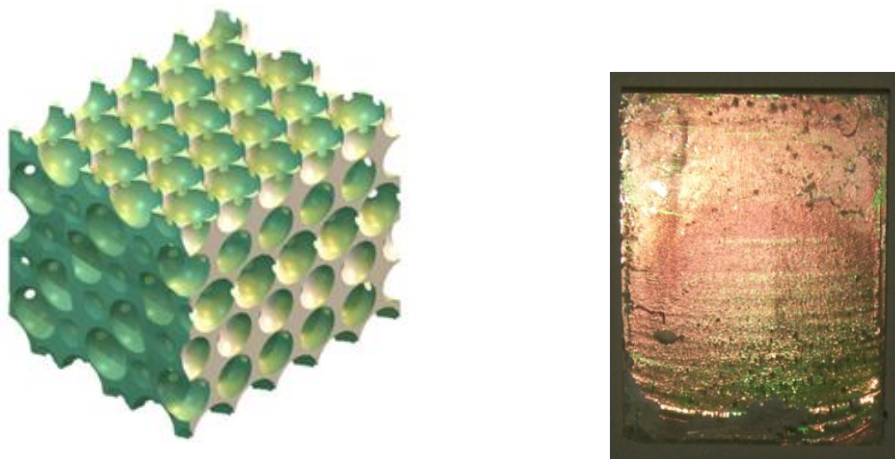


Figure 3-4: Inverse opal *fcc* crystal; top of crystal is the (111) plane and left side is (220). Iridescent (111) specular reflection off a TiO_2 infiltrated *fcc* colloidal crystal on polymer.

Diffraction of light waves inside a 3D-PC is most easily understood by adapting the Laue method for x-ray diffraction of crystals.²⁷ Instead of spherical wave fronts occurring as a result of electron absorption and emission of x-ray, or Rayleigh scattering, the spherical wave fronts occur between the high refractive index scattering centers. Various order diffraction cones form at the

intersections of the spherical wave fronts along a periodic row of scatter centers. And, at the intersection of the three diffraction cones coaxial with three non-coplanar rows of scattering centers two diffraction lines per conical intersection arise.

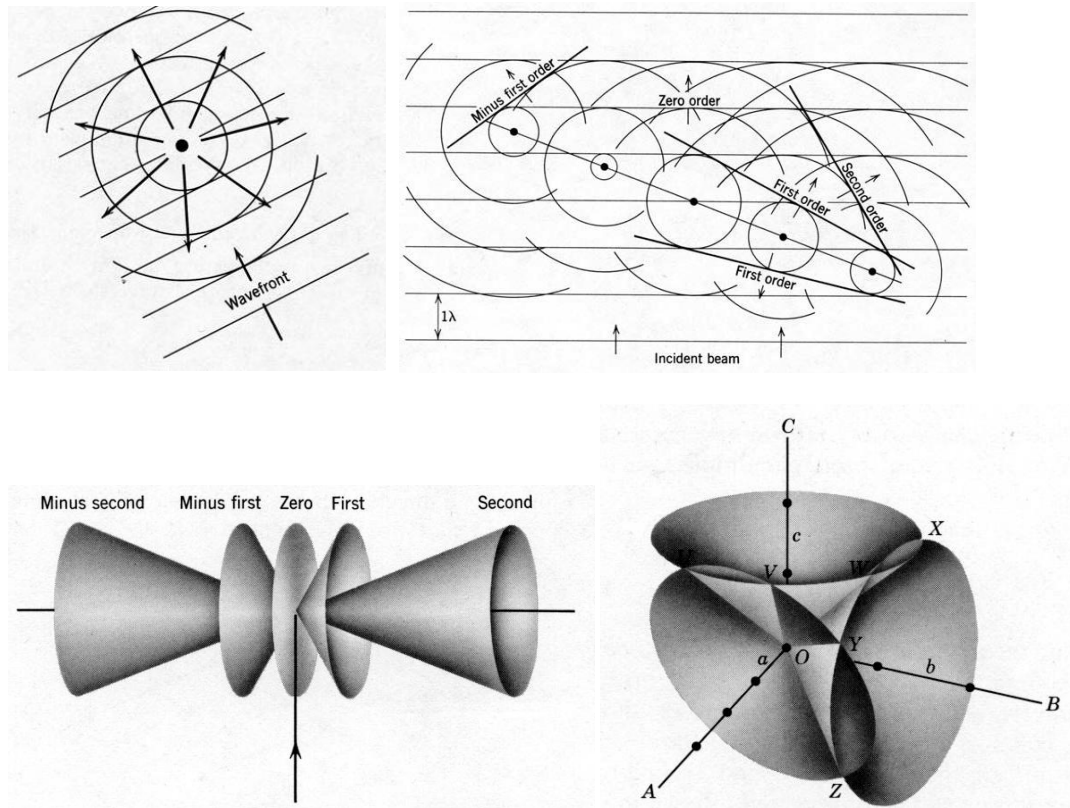


Figure 3-5: Depiction of 3D-PC diffraction cone formation and intersection.

After a substantial number of consecutive diffractions a range of light waves are forbidden in the 3D-PC along that direction. If that range of light waves is forbidden, $DOS = 0$, in all directions, a PBG exists for that 3D-PC. If propagation along all directions is not forbidden a stop band, or pPBG, exists. Generally for a PBG to appear, the contrast between the two refractive indices must be $\Delta n \geq 2$. When lower, however, a stop band or a pPBG can still appear in a 3D-PC. In this study an anatase TiO_2 inverse opal filled primarily with acetonitrile will be used; in this 3D-PC a pPBG forms. Accordingly, the $\Delta n \approx 2.54 - 1.35 = 1.19$.

Additionally photons that have energies near an edge of a stop band will, because of dispersion relation, resemble a standing wave as its group velocity is close to zero, $v_G = \frac{d\omega}{dk} \cong 0$; Figure 3-6. Inside the 3D-PC the confinement of these slow photons resembles an oscillating string between two fixed points. Those electromagnetic waves near the blue edge of the stop band oscillate with nodes at the high refractive index material, i.e. semiconductor. Conversely waves oscillating in the 3D-PC with frequencies near the red edge of the stop band have nodes at the low refractive index material, i.e. redox couple medium. Thus electric field enhancement occurs at both edges of the stop band but in opposing media.

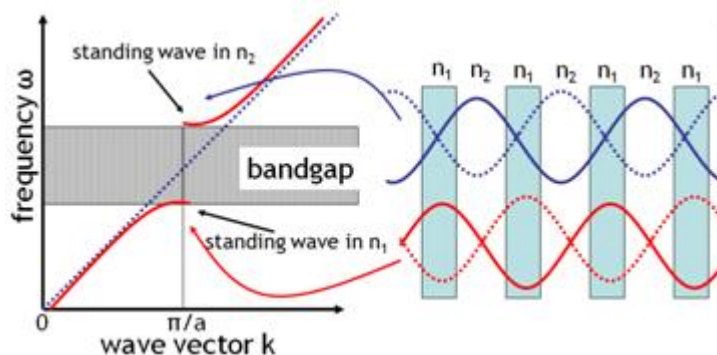


Figure 3-6: Standing waves at blue and red edges of the forbidden gap at the 1st Bragg plane for light with normal incidence.

3.3. Strategies for Building bi-DSSCs

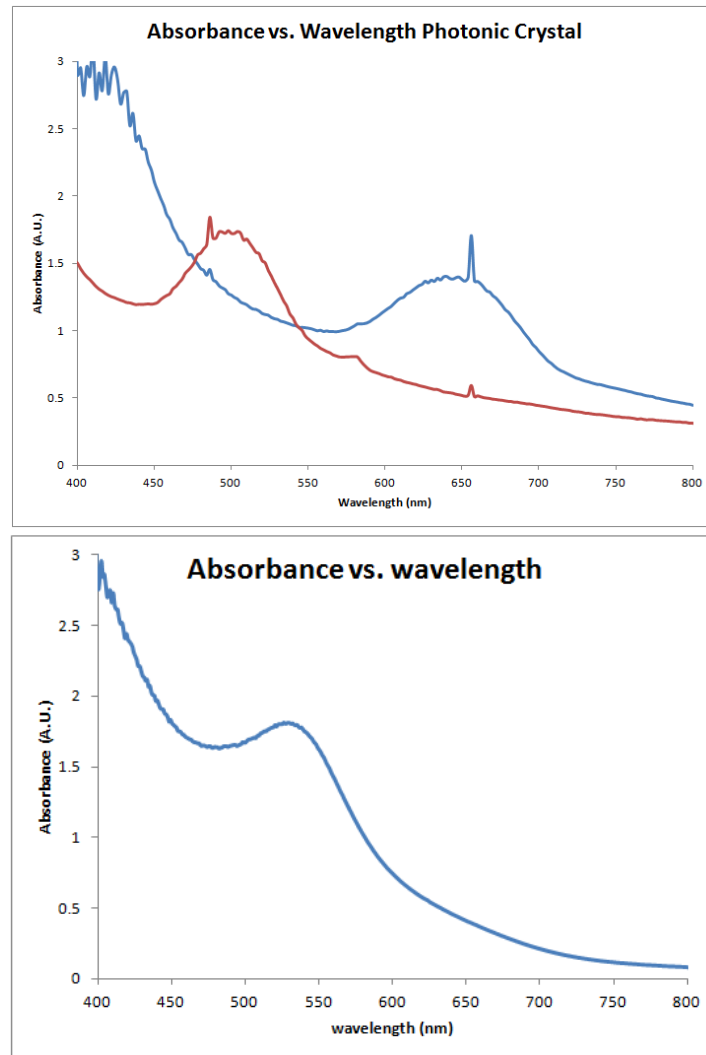
The largest innovation a bi-DSSC provides that a 3D-PC DSSC cannot is utilizing the back-reflected light from the 3D-PC's stop band. A 3D-PC DSSC must therefore be designed so that the light within its stop band is not missed. In a bi-DSSC, on the other hand, a sensitizer's capability to capture more of the solar spectrum within the stop band is a prudent aim. Boosting N719's absorbance of a 580 to 700nm range of light, for example, would amplify its spectral response into orange and red light; Figure 2-11, Section 2.4. Sensitizers, such as N719, are unable to effectively harvest the far visible and near IR ranges of light which comprises about 50% of the

sun's power. Tailoring the 3D-PC's stop band to N719 requires, therefore, centering it at 640nm; the center of the pPBG along the (hkl) plane can be estimated by the following equation:

$$\lambda_{hkl} = 2d_{hkl}n_{\text{eff}}\sqrt{1 - \sin^2\{\beta - \arcsin(\sin\theta/n_{\text{eff}})\}} \quad [11]$$

$$\lambda_{111} = 2d_{111}(n_{\text{eff}}^2 - \sin^2\theta)^{1/2} \quad [12]$$

$$n_{\text{eff}} = f_1n_1^2 + f_2n_2^2 \quad [13]$$



(Above) absorbance spectra of ~240nm (red) and ~320nm void diameter TiO_2 in ethanol inverse opals. There are worn photodiodes in the spectrophotometer that give erroneous narrow peak at 480 and 660nm; these should be ignored. (Below) ~320nm TiO_2 in air inverse opal. The λ_{hkl} red shifts when the ethanol infiltrates the inverse opal because the n_{eff} increases. Note: substrate absorbance has been subtracted from each spectrum.

Figure 3-7: Absorption curve for 300 and 400nm Inverse Opals.

Notice in Equations 6-8 how the λ_{hkl} changes proportionally with n_{eff} . The top spectrum of the 320nm void diameter inverse opal ($d_{111} = \text{void dia} \times 0.816$) in ethanol demonstrate how much the stop band peak is blue-shifted, λ_{hkl} decreases, when n_2 decreases from ~ 1.3 to 1.0 . It should also be noticed that at $l_{\text{mfp}} = 320\text{nm}$ of the 3D-PC should enhance N719 dye absorbance in light range to the red of the dyes absorbance peak without an inverse opal component. Figure 3-13 is a photograph of a 320nm void diameter inverse opal. The orange-yellow iridescence indicates that the 620 to 640nm light waves are effectively back-reflected by this inverse opal.

3.4. Choice of bi-DSSC Materials

The following DSSC components were kept standard for all cells tested in order to better isolate the optical effects of the bi-DSSC: N719 dye, ~ 20 nm diameter hydrothermally treated ncTiO₂ particles (recipe in Section 2.5.X); I/I₃⁻ redox pair, 8Ω/sq FTO coated glass for photoanode; Pt evaporated on 15Ω/sq FTO coated glass and further platinized with H₂PtCl₆ for photocathode; and, TiO₂ inverse opal template from polystyrene spheres.

3.5. Experimental bi-DSSC Attempts

The second route was used by Hwang *et al.* to successfully produce bi-DSSCs; after the colloidal template was deposited onto a calcined and sintered meso layer, the template was infiltrated with TiO₂ with ALD. Although bi-DSSCs with reasonable light-to-power efficiencies ($\eta \approx 8.2$) had been fabricated, the same efficiency can be achieved without any scattering layer.

It was determined that controlling the surface of the meso layer before depositing the sacrificial colloidal crystal template. By depositing Al₂O₃ over the top of the interstices of the meso layer's outer surface, the colloidal crystal template could then be deposited directly onto the

meso film and followed by template infiltration. Various infiltration methods were tested. Infiltration using capillary forces to draw ncTiO₂ particles (length about 6nm) up into the template interstices gave excellent results. Although porous with a reduced effective refractive index, infiltration of the template was very complete and not hollow as is liquid phase infiltration (80% or less of the interstitial space are filled). Also, due to its already crystalline morphology, the ncTiO₂ filled inverse opal film contracted 4 times less than sol-gel filled opal films upon heating and cooling.

Once these composite films (described in Section 1.2) are successfully constructed with the ability to control variations, so that reliable experimental evidence is collected, it is hypothesized that by intentionally altering specific physical characteristics of the bi-layer composite structure, the nature of distinct light localization and resonance effects would be elucidated. For example, when an overlayer on the surface of a 3D-PC facing the incoming light is present, it can become a 2-D grating as shown in Figure 3-8(a). Resultantly excitation of surface waves (that are standing waves or waves guided within the grating's grooves) form surface plasmon resonances or polaritons for a small range of incident p-polarized light; these are called Wood anomalies. These modes can prevent coupling of photons (whose energies are within and near the stop band) to the 3D-PC. When this happens electric fields within the 3D-PC do not form.²⁸ However, when this photon siphoning overlayer is removed so that the top layer forms hemispherical voids, as in Figure 3-8(b), Wood's anomalies are eliminated and expected electric fields in the 3D-PC are present. A fabrication method that allows surface modification of a 3D-PC (via reactive ion etching (RIE) or ion milling) prior to 3D-PC/meso nc-nSC fusion would enable the investigation of several interesting questions: how is the light harvesting efficiency of the bi-DSSC affected by the 3D-PC/meso nc-n-SC interface; can the presence or lack of presence of Wood anomalies be detected if a bi-DSSC with an overlayer is compared to one without the

overlayer; are the electric fields generated within the 3D-PC that significant since its specific surface area is about a third of a typical meso nc-n-SC's?

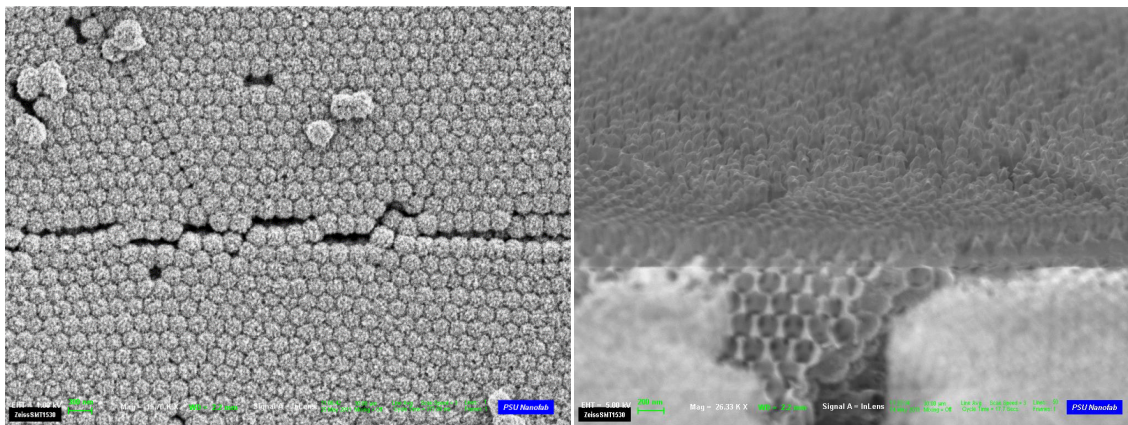


Figure 3-8: (a) Overlayer on top of TiO_2 inverse opal (1,1,1) surface (top view). (b) Complete TiO_2 overlayer removal by ion milling (side view).

As discussed in Section 1.2, the majority of incident light waves whose paths are manipulated when interacting with a 3D-PC have energies in and near its stop band. Most of the forbidden electromagnetic waves are coherently backscattered and form an enhanced intensity cone in the backscattering (CBS) direction within the meso layer. The appearance of a highly saturated and vibrant hue on the surface of a 3D-PC is evidence of the CBS; although Wood anomalies can create this iridescence as well.

Since the cone of CBS propagates first through the meso layer, its structure must be considered. And since the absorption of light by the meso nc-n-SC layer has been shown to benefit greatly from this when the peak of the stop band is centered appropriately to the sensitizer, the question arises: how can the meso film be structured so that it maximally benefits from the coherent, and incoherent, Bragg scattering? There are many possible routes to explore this question.

Of course the front layer, the sensitized meso nc-n-SC film, absorbs the majority of light waves within the sensitizer's absorption spectrum. This then lowers the intensities of light waves entering the 3D-PC layer that correspond to higher molar absorptivities in the sensitizer.

However, since the main function of the 3D-PC is to enhance the absorbance via lengthening the path lengths of those light waves which correspond to lower molar absorptivities in the sensitizer (especially to the red side of its peak absorbance), the loss of light waves absorbed by the sensitized meso layer does not matter as long as the meso layer's thickness accommodates optimal light absorption about its peak absorbance frequencies. In fact, the 3D-PC's specific surface area is almost three times less than that of a typical DSSC meso layer. Thus it should not be considered a primary absorber layer since it cannot produce as much photocurrent as the meso nc-n-SC film.

According to the superposition principle when each layer composing the bi-DSSC photonic system can operate separately at given efficiencies, the two could compositely operate at the sum of these two efficiencies when effectively connected. For example, when a sensitized 3D-PC photoanode cell operating at $\eta = 4.5\%$ is combined with a separate meso-ncTiO₂ photoanode DSSC generating electricity at $\eta = 6.5\%$ into a single photoanode, the bi-layer cell's efficiency should be 11%, or perhaps more if a synergy exists. But the 3D-PC must not absorb the light which the meso nc-n-SC can do more efficiently.

The superposition principle has been demonstrated in multi-junction solid state PVs. However this principle has not been demonstrated before in bi-DSSCs. It follows that developing a reliable construction recipe for producing mechanically joined bi-DSSCs with variable pPBGs is prudent before testing superposition of the layers' efficiencies. When light whose energy lies within the stop band tries to propagate through the 3D-PC, the light is scattered incoherently and/or coherently back out from where it came. Some of this back-reflected light is thought to be captured in effective resonant cavities created within the mesoporous film. Under this condition optical energy would be temporally and spatially confined. Understanding the conditions in which this type of resonance effect occur in a bi-DSSC, therefore, would bridge to more effective

light trapping; especially since confined propagation occurs in or near the bi-DSSC layer that is most densely populated with sensitizer molecules.

3.5.1 Inverse Opal Fabrication

The 3D-PC fabrication process begins with making a sacrificial *fcc* colloidal crystal of sub-micron diameter spheres (typically polymer). The interstices of the template crystal are then infiltrated with a metal oxide material. Infiltration can be accomplished via a metal oxide precursor sol-gel or a colloidal solution of small nc-n-SC particles. The interstices create capillary forces to draw up the sol or colloidal solution up into the interstices. As the sol or colloidal solution evaporates at the edges the particles in these solutions are crystallized and drawn together.

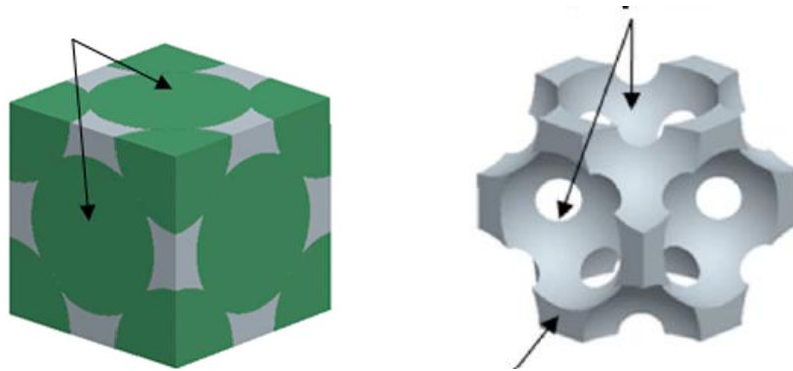


Figure 3-9: Unit cell for *fcc* crystal. Inverse opal *fcc* unit cell; this is called the backbone.

To deposit the sacrificial *fcc* colloidal crystal the most favorable method is vertical evaporative deposition. Near the surface of the colloidal solution small groups of spheres form. At the bottom of the meniscus of the substrate, these groups are forced into closer proximity; Figure 1-2. Subsequently, at the top of the meniscus evaporation of the colloidal solvent in the interstices of the spheres creates capillary forces which draw the spheres into a close packed crystal along the plane of the substrate. Heat is typically used to control the evaporation rate; in this study deposition temperature of 55°C was employed. When accidentally placing two

substrates that were stuck to one another into a crystal deposition chamber, it was noticed that a very homogenous and planar colloidal crystal formed in between these substrates. Capillary vertical deposition has since proven to be a very reliable method for template deposition. This method is particularly attractive since the capillary thickness and hence the colloidal crystal thickness and shape is very controllable.

The resultant colloidal crystal, which adsorbs onto the substrate, must be sintered at 90°C and infiltrated with a sol-gel or small nc-TiO₂ particles. The latter infiltration process is less detrimental to crystal's stability on the substrate. The typically low pH of a metal-oxide sol-gel changes the electrostatic forces between the polymer spheres. This flaking effect can be seen in Figures 3-2, 3-13, 3-15 and 3-16. On the other hand, the infiltration process occurs at a neutral pH and can be expedited by placing a glass slide over the crystal and just submerging the bottom of this slide-slide capillary. With a blow dryer or placing the sample inside a convective oven the rate of infiltration is significantly increased compared to room temperature nc-TiO₂ colloid infiltration.

In this study a decal method was pursued for connecting the 3D-PC slab to the meso nc-TiO₂ film. This process involves making the two films separately and then pasting them together with a meso nc-TiO₂ paste. In order to facilitate easy removal of the substrate from the colloidal crystal after ensuring connectivity between the meso nc-TiO₂ and 3D-PC layers, a polymer film was spin-coated onto the substrate prior to the two-step crystal deposition process. The film was subsequently kept in the deposition oven to keep the tension on the film constant. A dilute solution of poly vinyl acetate (PVAc) was found to successfully allow good crystal adsorption, infiltration under sol-gel and nc-TiO₂ conditions and facile removal of the substrate. The SEM image of a typical, TiO₂ infiltrated 3D-PC template made of surface modified polystyrene spheres is shown in Figure 3-10. As seen in this Figure good adsorption of the crystal to the PVAc film was somewhat tenuous when the template infiltration process involved soaking the crystal

template in a TiO_2 sol-gel. In Figure 3-10 flecks of 3D-PC can be seen; these are a result of poor adsorption onto the PVAc or swelling of the PVAc during vertical evaporative deposition or sol infiltration of the colloidal crystal and are seen after sol-gel infiltration.

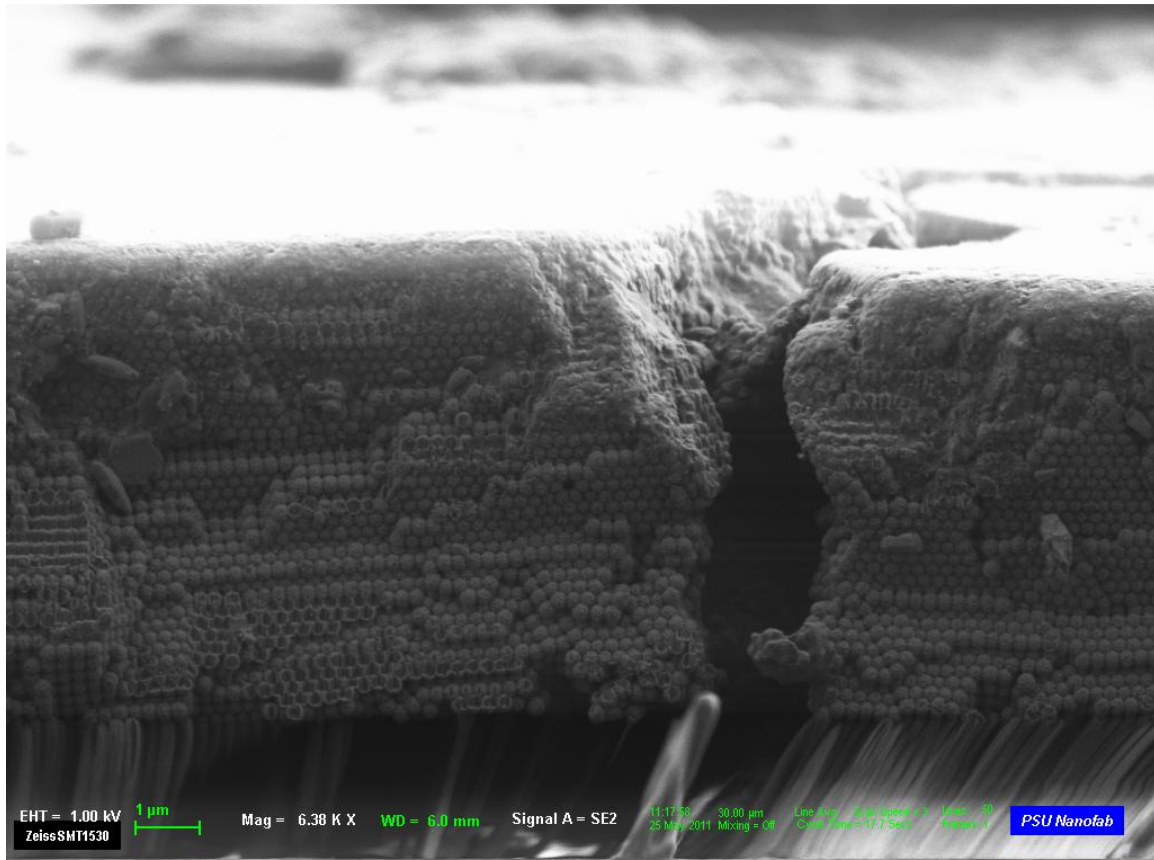


Figure 3-10: TiO_2 Sol-gel infiltrated colloidal crystal after RIE treatment.

Also seen in Figure 3-10, and more clearly in Figure 3-12(a), is a polymer overlayer formed after RIE etching the TiO_2 overlayer. Ion milling was used as an RIE alternative. As seen in Figures 3-10 and 3-11 the ion milling process was more effective at taking away the polymer spheres of the crystal template. However controlling amount of TiO_2 backbone removed during this process proved difficult. In Figure 3-13(c) peeling of the crystal from the polymer coated substrate can be seen. This problem resulted from excessive heat generated by the Ar ion plasma.

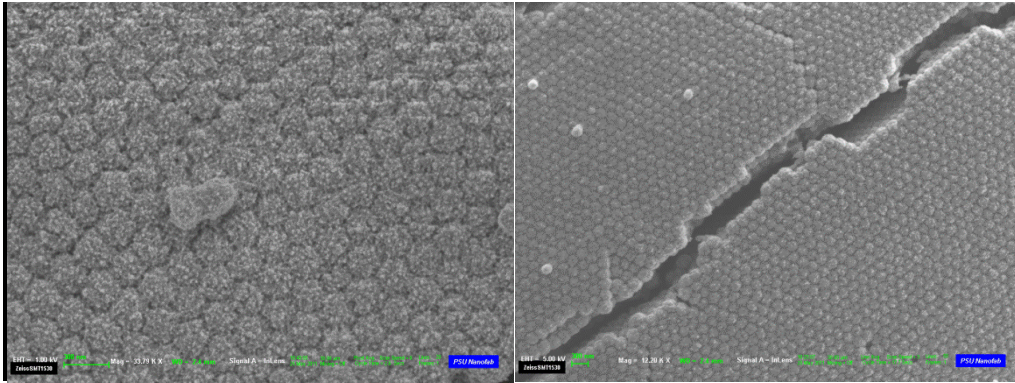


Figure 3-11: (a) IO top before RIE. (b) 45 sec RIE.

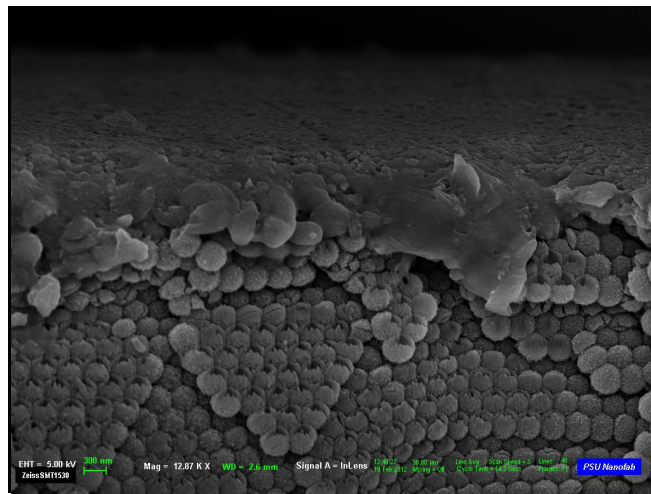
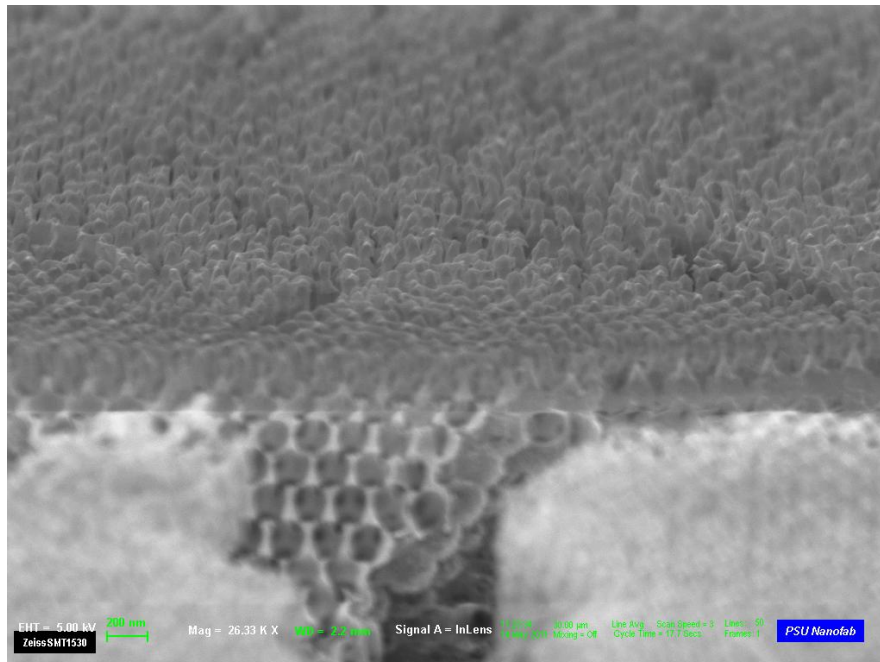


Figure 3-12: (a) IO top before RIE. (b) 45 sec RIE.



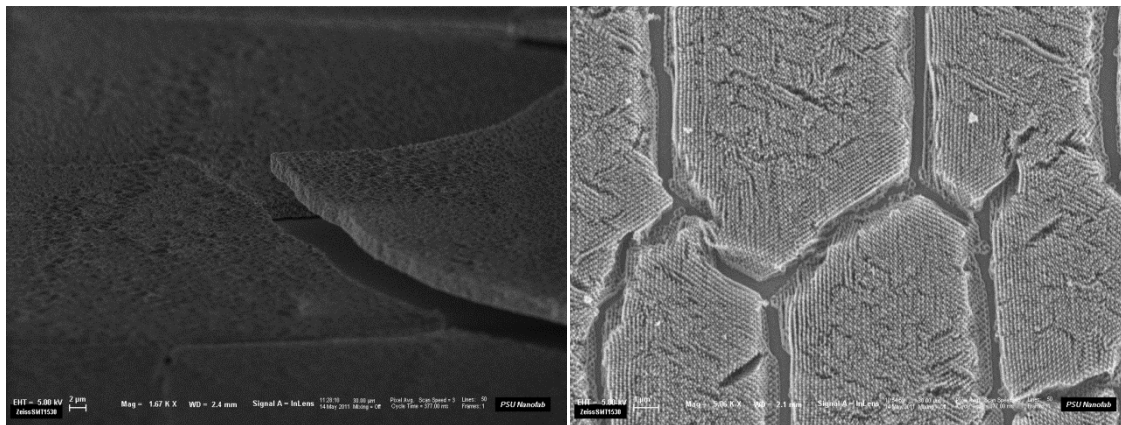


Figure 3-13: Ion milled.

The RIE process proved to be more effective than the ion milling. The sample holder was cooled so there was no crystal peeling. Recipes for an oxygen plasma treatment after the fluoride plasma etch was complete was being developed. The optimum time for etching the TiO_2 overlayer with the RIE was 30 seconds. A bi-DSSC was fabricated using a 240nm void diameter inverse opal decal. As seen in Figures 2-13 an inverse opal was not optimal for enhancing N719's absorbance of the sun's spectrum, however it proved a good sample for testing the decal fabrication process. This process will be further described in the following section.

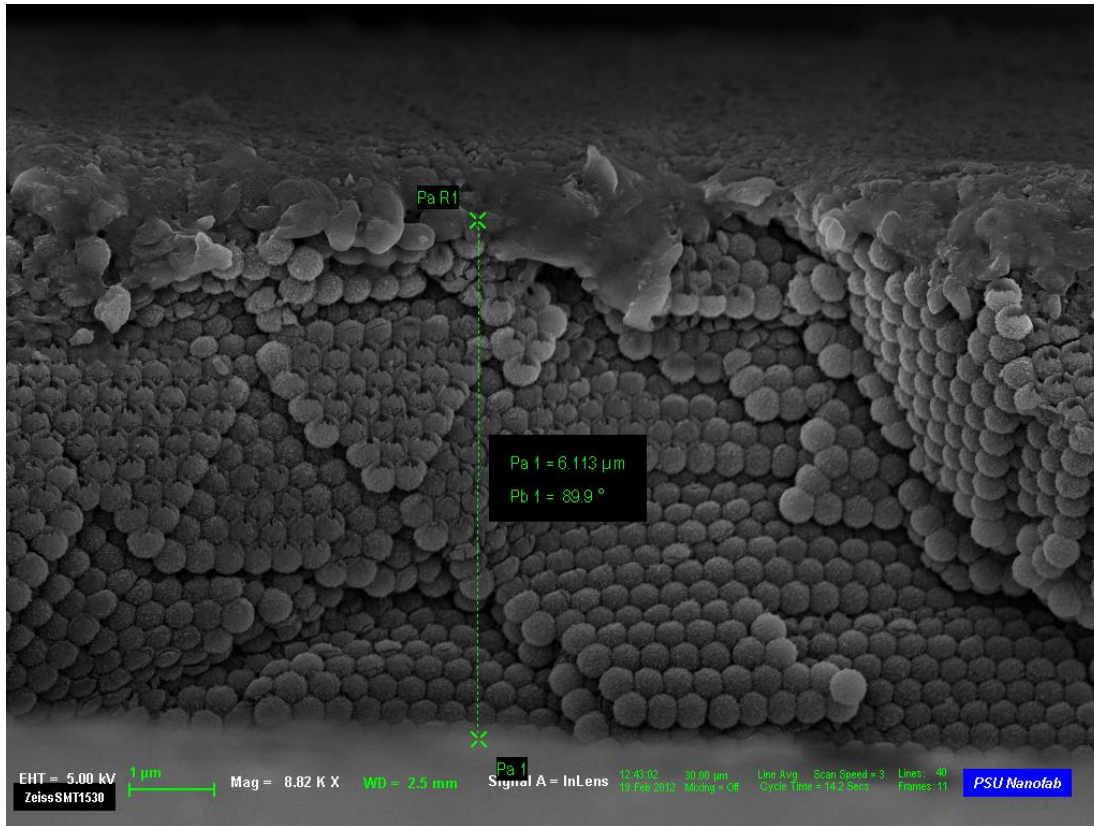


Figure 3-14: 45sec RIE sol-gel infiltrated PS colloidal crystal

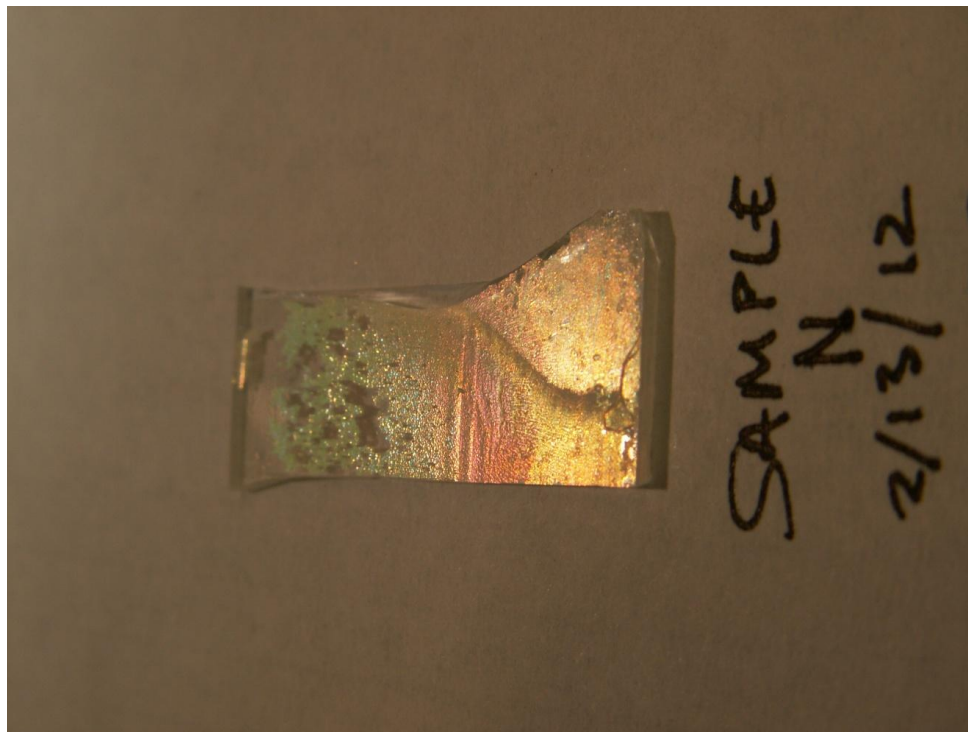


Figure 3-15: 320nm void diameter inverse opal on PVA; RIE 30 sec. Before decal transfer.

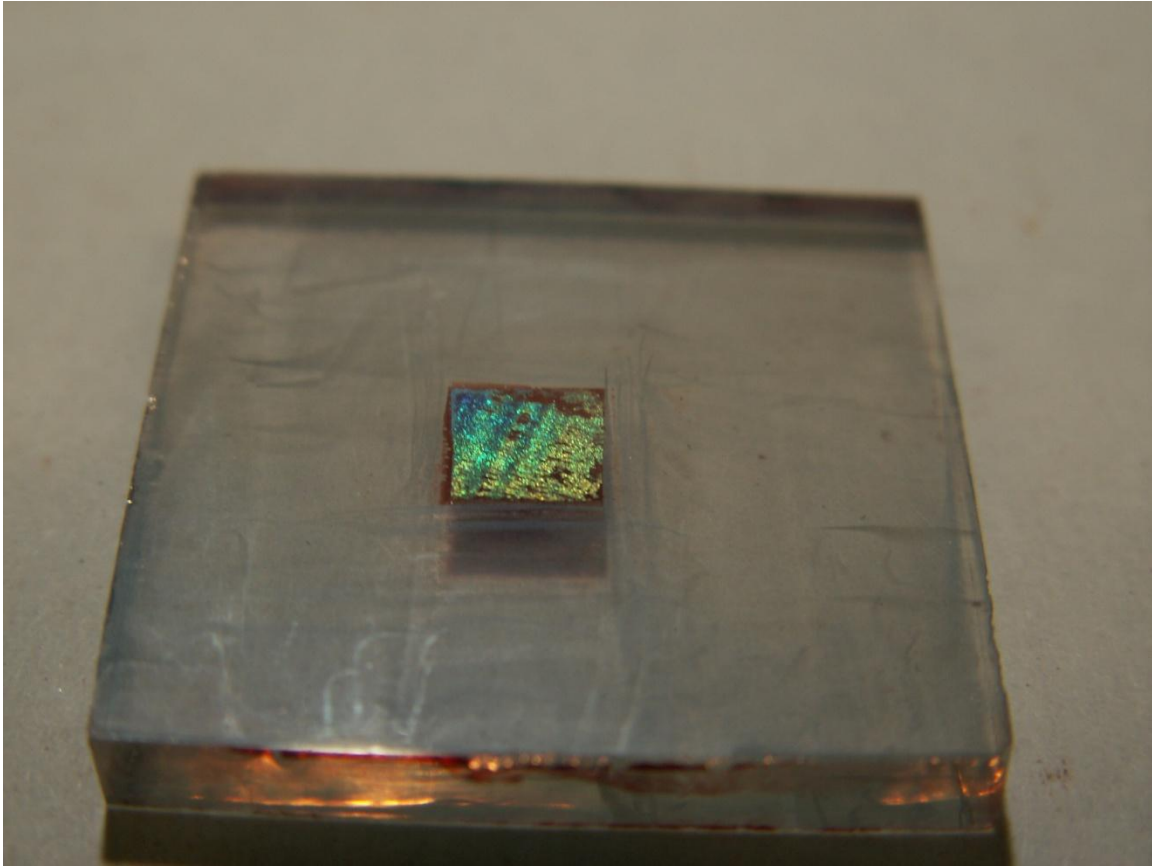


Figure 3-16: 320nm void diameter bi-DSSC

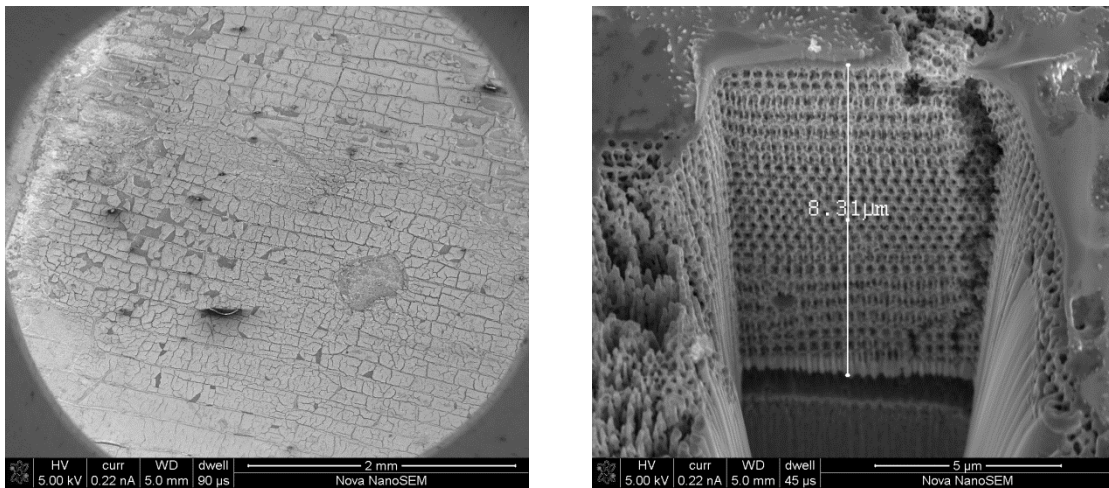


Figure 3-17: a) IO layer decal film sintered to meso nc-TiO₂ layer. (b) FIB trenching

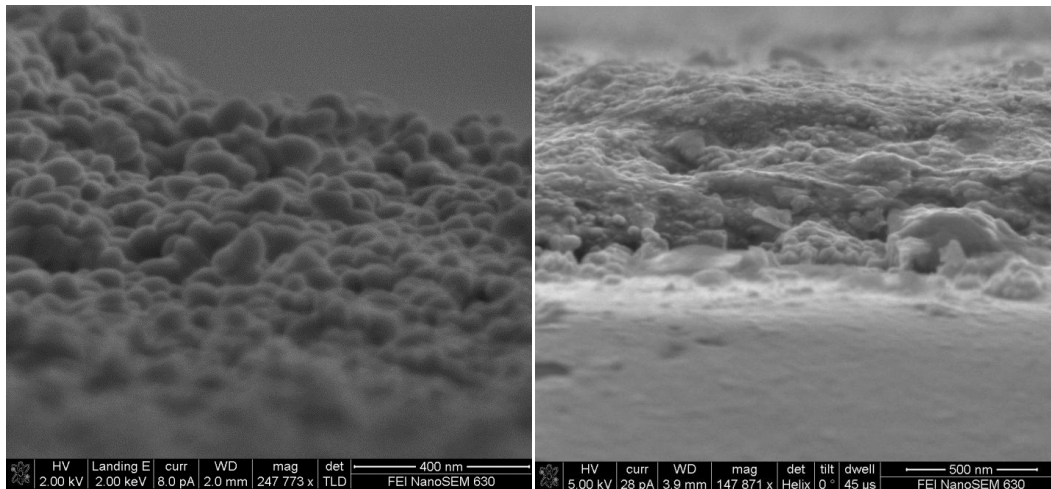


Figure 3-18: Spin coat nc-Al₂O₃/nc-TiO₂ 1:1 mix.

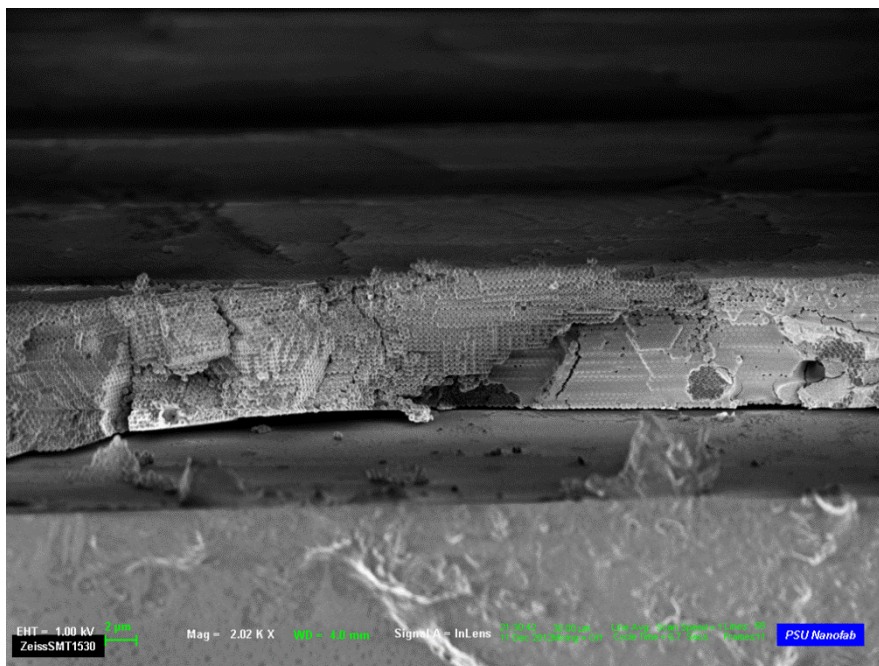


Figure 3-19: Sandwiched PC template infiltrated with 6-10nm nc-TiO₂ particle colloidal solution.

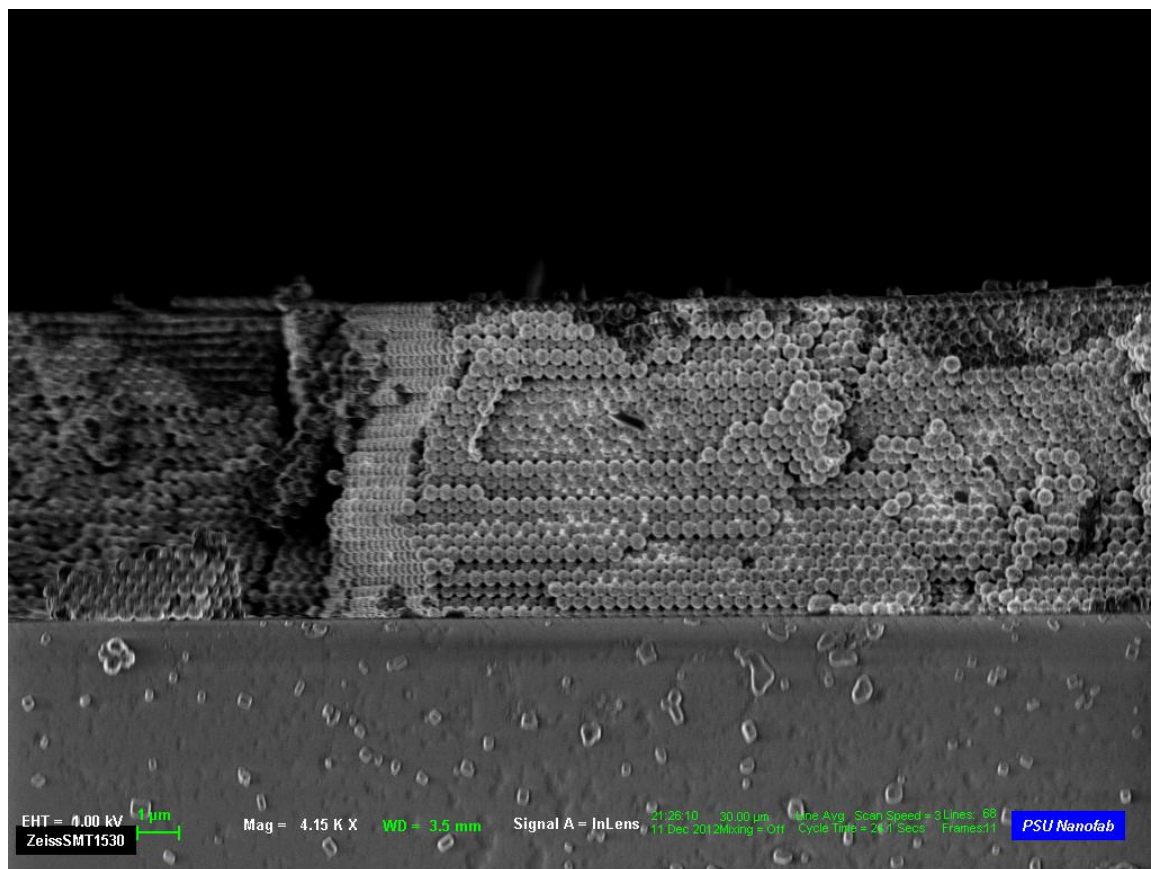


Figure 3-20: PC template infiltrated with 6-10nm nc-TiO₂ particle colloidal solution.

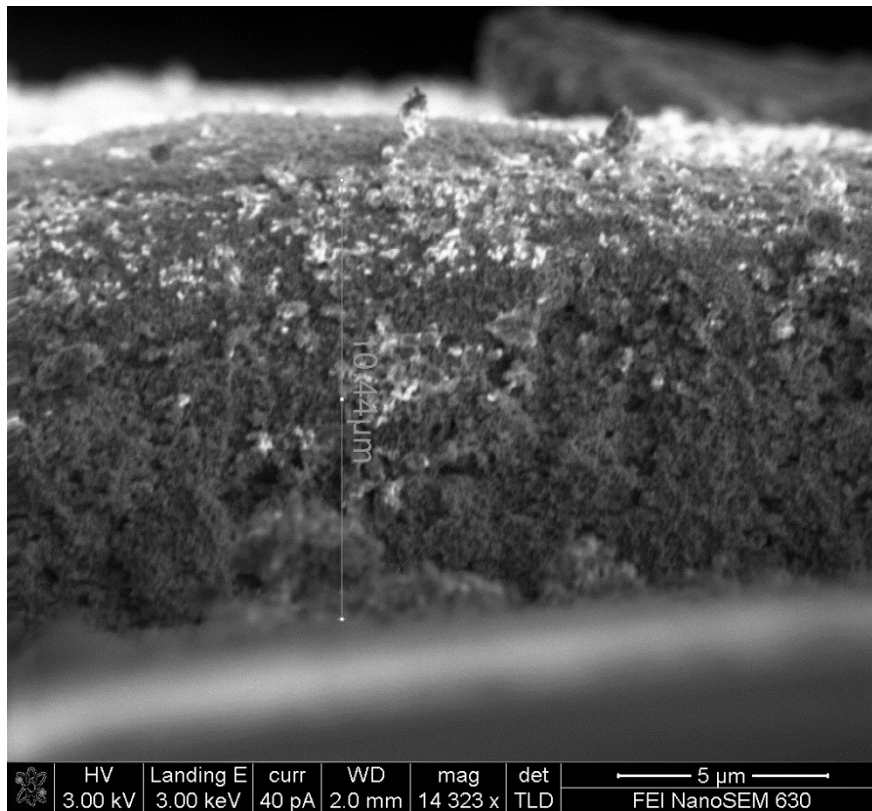


Figure 3-21: Screen print nc-Al₂O₃/nc-TiO₂ 1:1 mix w/ binder.

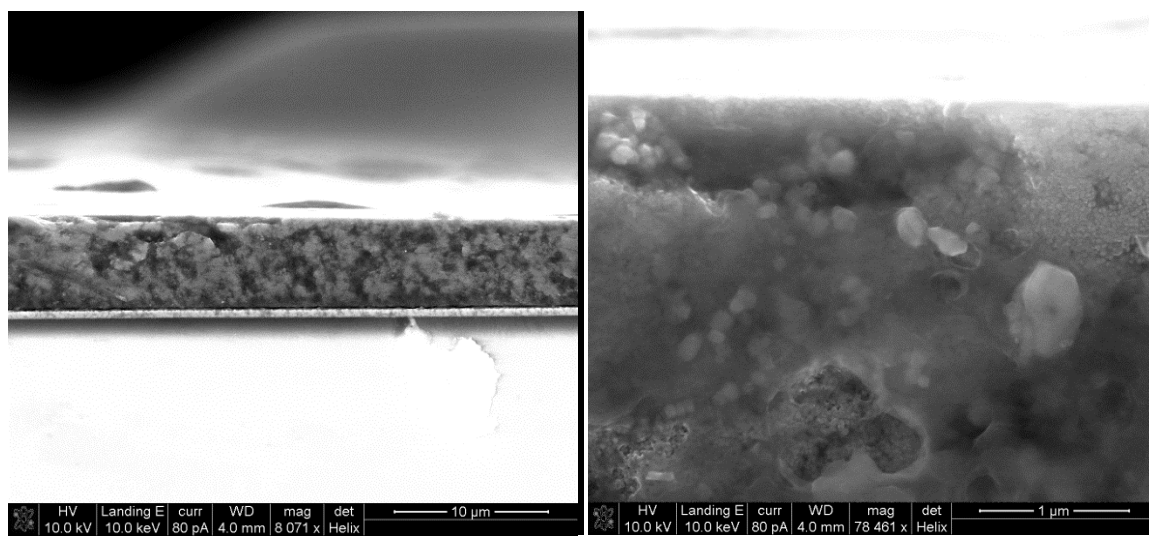


Figure 3-22: Meso-ncTiO₂ layer coated with Al₂O₃ by ALD (500 cycles).

3.6. Conclusions and Future Work

In this work very complex and heavily laden with nomenclature description of DSSC function and construction was simplified so that DSSC experimentation can be utilized due to its low cost and ease of fabrication in the laboratory. Ideas of robust fabrication of bi-DSSC were explored with the hope of finding a versatile and thereby useful technique for exploring 3D-PCs in PVs. Although not yet tested, it is believed that an Al_2O_3 protective coating on the meso layer prior to colloidal crystal deposition and infiltration will provide an excellent bi-DSSC method. Also not tested is the idea of attaching a milled 3D-PC, so that Wood's anomalies can be explored in bi-DSSCs, to a meso layer via a recently developed technique involving a sol-gel that crystallizes well on nucleation crystals and surfaces to form a mesoporous film within sub-micron confined spaces.

One of the most interesting effects of coherent Bragg scattering is the interference of incident and reversed light path. This is called slow photon propagation. The dispersion relation causes slowing of photons and thereby constructive interference at the edges of the stop band. At the blue edge the nodes are at the scatter centers. But since IOs made with ncTiO_2 particles are porous, the electric field in the cavity extends into the dyed ncTiO_2 particles. This idea has not been explored at all in bi-DSSCs

Anderson localization in 3D-PCs is another means of trapping light. Analogous to electrons in an amorphous crystalline semiconductor, the light is slowed due to the lack of periodicity. Although the problem has been somewhat explored by Chen *et al.* for IO films, it has not been explored using bi-DSSCs with any degree of reproducibility.

The main problem encountered during experimentation, nevertheless, was the elusiveness of And since the specific challenges of developing a fabrication method for reproducible bi-DSSCs were not sufficiently overcome, no experimental contributions were made towards understanding bi-DSSC/light mode relationships. Nonetheless it would greatly facilitate the

ensuing study. Subsequently this platform would enable one to draw more definitive correlations between a bi-DSSC's capability to harvest light and its various physical characteristics.

Appendix A

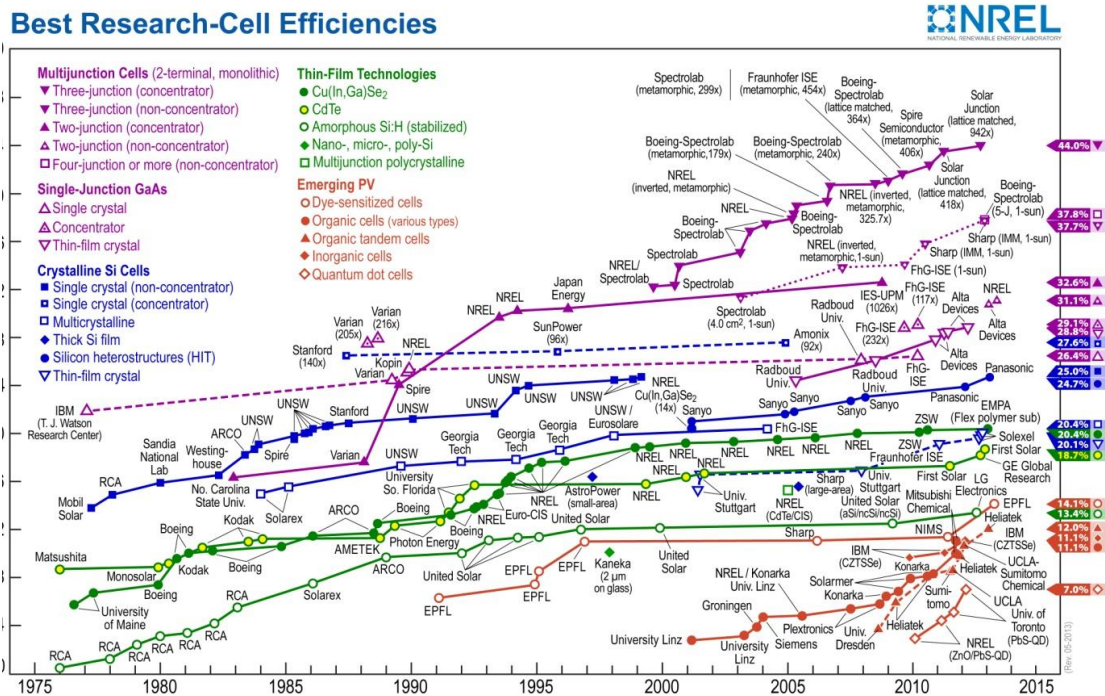


Figure A-1: Advances in solar cell types: Efficiency versus year chart, from Ref 11.

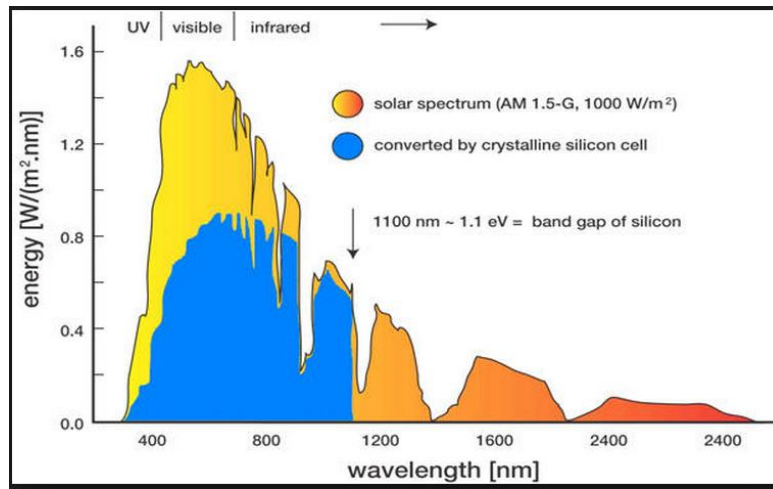


Figure A-2: Absorption Spectrum of N719 Dye

References

- ¹ Denman, K.; Brasseur, G.; Chidthaisong, A.; Ciais, P.; Cox, P.; Dichenson, R.; Hauglustaine, D.; Heinze, C.; Holland, E.; Jacob, D.; Lohmann, J.; Ramachandran, S.; da Silva Dias, P. 2007: Couplings Between Changes in the Climate System and Biogeochemistry. In *Climate Change 2007: The Physical Science Basis. Contribution of Working Group I to the Fourth Assessment Report of the Intergovernmental Panel on Climate Change*; Solomon, S., Qin, D., Manning, M., Chen, Z., Marquis, M., Averyt, K., Tignor, M., Miller, H., Eds.; Cambridge University Press, Cambridge, United Kingdom and New York, N.Y., U.S.A., 2007, p 512.
- ² Wenger, A.; Orttung, R.; Perovic, J. *Energy and the transformation of International Relations, Toward a New Producer-Consumer Framework*; 2nd ed., Oxford University Press for the Oxford Institute of Energy Studies, Oxford, United Kingdom and New York, N.Y., U.S.A., 2009, pp 1-23.
- ³ <http://www.energies-renouvelables.org/observ-er/html/inventaire/pdf/14e-inventaire-Chap01-Eng.pdf>
- ⁴ <http://www.eia.gov/electricity/annual/archive/03482009.pdf>
- ⁵ http://www.eia.gov/forecasts/aeo/electricity_generation.cfm
- ⁶ <http://www1.eere.energy.gov/geothermal/pdfs/ngap.pdf>
- ⁷ <http://pubs.usgs.gov/fs/fs-0113-01/fs-0113-01textonly.pdf>
- ⁸ <http://www.kpmg.com/Global/en/IssuesAndInsights/ArticlesPublications/Documents/taxes-incentives-renewable-energy-2012.pdf>
- ⁹ U.S. Department of Energy.
http://www4.eere.energy.gov/solar/sunshot/resource_center/sites/default/files/solar-powering-your-community-guide-for-local-governments.pdf (accessed April 1, 2013)
- ¹⁰ Wei, T.; Lan, J.; Wan, C.; Hsu, W.; Chang, Y. Fabrication of Grid Type Dye-Sensitized Solar Modules with 7% Conversion Efficiency by Utilizing Commercially Available Material. *Prog. Photovolt.: Res. Appl.* [Online] **2012** doi: 10.1002/pip.2252
- ¹¹ NREL: National Center for Photovoltaics. <http://www.nrel.gov/ncpv/> (accessed June 1, 2013)
- ¹² Hardin, B.; Snaith, H.; McGehee, M. The Renaissance of Dye-Sensitized Solar Cells *Nature Photonics* **2012**, 6, 162-169.
- ¹³ Hwang, D; Lee, B.; Kim, D. Efficiency Enhancement in Solid Dye-Sensitized Solar Cell by Three-Dimensional Photonic Crystal *RSC Adv.* **2013**, 3, 3017-3023
- ¹⁴ Yan, K.; Qui, Y.; Chen, W.; Zhang, M.; Yang, S. A Double Layered Photoanode Made of Highly Crystalline TiO₂ Nanooctahedra and Agglutinated Mesoporous TiO₂ Microspheres for High Efficiency Dye-Sensitized Solar Cells. *Energy Environ. Sci.* **2011**, 4, 2168-2176
- ¹⁵ Tetreault, N.; Arsenault, E.; Heiniger, L.; Soheilnia, N.; Brillet, J.; Moehl, T.; Zakeeruddin, S.; Ozin, G.; Gratzel, M. High Efficiency Dye-Sensitized Solar Cell with Three-Dimensional Photoanode. *Nano Letters* **2011**, 11, 4579-45884
- ¹⁶ Lee, M.; Teuscher, J.; Miyasaka, T.; Takurou, M.; Snaith, H. Efficient Hybrid Solar Cells Based on Meso-Supersaturated Organometal Halide Perovskites *Science* **2012**, 338, 643-647
- ¹⁷ Lango, C.; De Paoli, M. Dye –Sensitized Solar Cell: a Successful Combination of Materials *J. Braz.Chem. Soc.* **2003**, 14(6), 889-901
- ¹⁸ Fonash, S *The Physics of Photovoltaic Devices*
- ¹⁹ Turrion, M.; Bisquert, J.; Salvador, P. Flatband potential of F:SnO₂ in TiO₂ Dye-Sensitized Solar Cell: An Interference Reflection Study *J. Phys Chem. B* **2003**, 107,9397-9403
- ²⁰ Watson, D. Meyer, G. Cation Effects in Nanocrystalline Solar Cells *Coordination Chemistry Reviews* **2004**, 248,1391-1406.
- ²¹ Ito, S.; Muakami, T.; Comte, P.; Liska, P.; Gratzel, C.; Nazeeruddin, M.; Gratzel, M.; Fabrication of Thin Film Dye-Sensitized Solar Cells with Solar to Electric Power Conversion Efficiency over 10% *Thin Solid Films* **2008**, 516,4613-4619
- ²² Wu, M.; Tsai, C.; Wei, T. Electrochemical Formation of Transparent Nanostructured TiO₂ Film as an Effective Bifunctional Layer for Dye-Sensitized Solar Cells *Chem. Commun.* **2011**, 47, 2871-2873

-
- ²³ Wochnik, A.; Hanloser, M.; Durach, D.; Hartschuh, H.; Scheu, C. Increasing Crystallinity for Improved Electrical Conductivity of TiO₂ Blocking Layers *ACS Appl. Mater. Interfaces* **2013** [online]
DOI:10.1021/am401110n
- ²⁴ Li, L.; Diau, W. Porphyrin-Sensitized Solar Cells *Chem. Soc. Rev.* **2013**, 42, 291-304
- ²⁵ Shin, J.; Moon, J. Bilayer Inverse Opal TiO₂ Electrodes for Dye-Sensitized Solar Cells via Post-Treatment *Langmuir* **2011**, 27, 6311-6315
- ²⁶ Mihi, A.; Calvo, M.; Anta, A.; Miguez, H. Spectral Response of Opal-Based Dye-Sensitized Solar Cells *J. Phys. Chem. C* **2008**, 112, 12-17
- ²⁷ Connolly, J. Diffraction Basics
- ²⁸ Garcia-Santamaria, F.; Nelson, E.; Braun, P. Optical Surface Resonance May Render Photonic Crystal Ineffective *Phys. Rev. B* **2007**, 76, 075132